MOL.19990309.0403

QA:N/A

Civilian Radioactive Waste Management System
Management & Operating Contractor

Impact of Radioactive Waste Heat on Soil Temperatures

BA0000000-01717-5700-00030, Revision 0

March 4, 1999

Prepared for:

U.S. Department of Energy
Office of Civilian Radioactive Waste Management
1000 Independence Avenue S.W.
Washington, DC 20585

Prepared by:

TRW Environmental Safety Systems Inc.
1261 Town Center Drive
Las Vegas, NV 89134

Civilian Radioactive Waste Management System
Management & Operating Contractor

Impact of Radioactive Waste Heat on Soil Temperatures

BA0000000-01717-5700-00030, Revision 0

March 4, 1999

Prepared by:

Bruce A. Robinson, Earth and Environmental Sciences Division
Los Alamos National Laboratory

March 4, 1999
Date

Carl W. Gable, Earth and Environmental Sciences Division
Los Alamos National Laboratory

March 4, 1999
Date

Julian P. Lowman, Earth and Environmental Sciences Division
Los Alamos National Laboratory

March 4, 1999
Date

Approved by:

Charles D. Harrington, Earth and Environmental Sciences Division, Los Alamos National Laboratory

March 5, 1999
Date

INTENTIONALLY LEFT BLANK

This work was supported by the Yucca Mountain Site Characterization Office as part of the Civilian Radioactive Waste Management Program of the U.S. Department of Energy. This project is managed by the U.S. Department of Energy, Yucca Mountain Site Characterization Project.

The authors thank Kaylie Rasmuson for her collaboration in the collection and development of the soil-temperature data and George Zyvoloski for his technical review of the work. Finally, we give a special thanks to Roger Eckhardt for his assistance in preparing the document.

INTENTIONALLY LEFT BLANK

CONTENTS

Page

1. INTRODUCTION 1

2. MODELING APPROACH 2

   2.1 SITE-SCALE UNSATURATED-ZONE THERMOHYDROLOGIC MODEL 3
   2.2 ONE-DIMENSIONAL SOIL-ZONE MODEL 8

3. SITE-SCALE MODEL RESULTS 11

4. ONE-DIMENSIONAL SOIL-ZONE HEAT-TRANSFER MODEL RESULTS 25

   4.1 MODEL THEORY 25
   4.2 PRACTICAL MODEL CONSTRAINTS 30
   4.3 INVERSION OF TEMPERATURE-TIME SERIES DATA FOR SOIL THERMAL DIFFUSIVITY 31
   4.4 SUMMARY AND DISCUSSION OF SOURCES OF ERROR 36
   4.5 MODEL RESULTS 37

5. CONCLUSIONS 43

6. REFERENCES 46

APPENDIX: DETERMINATION OF DIFFUSIVITY A-1

INTENTIONALLY LEFT BLANK

FIGURES

Page

Figure 1. Map of Spatially Varying Infiltration Rate 4

Figure 2. Two-dimensional Antler Ridge Model Domain. 5

Figure 3. Normalized Heat Flux Due to Radioactive Decay Heat. 6

Figure 4. Unsaturated-zone Fluid Saturation. 12

Figure 5. Unsaturated-zone Temperature 13

Figure 6. Fluid-saturation Distribution Near Potential Repository 14

Figure 7. Saturation in Rock Near Two Emplacement Drifts 15

Figure 8. Temperature in Rock Near Two Emplacement Drifts 15

Figure 9. Relative Humidity in Rock Near Two Emplacement Drifts 16

Figure 10. Temperature in Rock Within the Repository 17

Figure 11. Temperature at the Top of the Calico Hills Unit 18

Figure 12. Spatial Variation of Heat Flux at the Surface After 1000 Years 19

Figure 13. Heat Flux Above Repository for Various Infiltration Rates 19

Figure 14. Heat Flux Above Repository for Two Heat-transfer Boundary Conditions. 20

Figure 15. Heat Flux Above Water Table (2-D Full Thermohydrologic, 2-D Heat Conduction Only, and 3-D Heat Conduction Only) 21

Figure 16. Simulated Heat Flux at Surface After 2000 Years (3-D Conduction Limited) 22

Figure 17. Heat Flux Above Water Table (2-D and 3-D Heat Conduction Only). 23

Figure 18. Temperature Below the Surface for a Diurnal Temperature Oscillation 27

Figure 19. Temperature Below the Surface for a Seasonal Temperature Oscillation 28

Figure 20. Temperatures for Wet-soil Thermal-diffusivity, Diurnal Temperature Variation 29

FIGURES (Continued)

Page

Figure 21. Temperatures for Wet-soil Thermal-diffusivity, Seasonal Temperature Variation 29

Figure 22. Air and Soil Temperature Measured Over a 14-day Period 32

Figure 23. Cross Covariance of Air Temperature to Soil Temperature 33

Figure 24. Cross Covariance of Air Temperature to Six Soil-temperature Time Series 34

Figure 25. Time Lag of Maximum Cross Correlation 35

Figure 26. Steady-state Soil-zone Temperature Profiles for Different Soil Wetness 38

Figure 27. Soil Temperatures for Dry Soil and Maximum Repository Heat Load 39

Figure 28. Soil Temperatures for Nominal Soil and Maximum Repository Heat Load 40

Figure 29. Soil Temperatures for Wet Soil and Maximum Repository Heat Load 41

Figure 30. Rise in Soil Temperature for Wet Soil at a 2-m Depth 42

TABLES

Page

Table 1. Soil Thermal Properties Used in Model Calculations 9

Table 2. Soil Thermal Diffusivities and Computed Heat-transfer Parameters 26

INTENTIONALLY LEFT BLANK

1. INTRODUCTION

Consideration of the impact of radioactive waste heat is necessary for many aspects of potential repository design. For example, thermohydrologic considerations near emplacement drifts impact the relative humidity, temperature, and the likelihood of dripping water on the waste packages, all of which in turn control the corrosion rate (Buscheck et al. 1996, p. 715). The solubility and speciation of radionuclides and the dissolution rate of the waste form itself are also strongly influenced by thermohydrologic considerations (Nitsche et al. 1994, pp. 3–5; CRWMS M&O 1995, pp. 4-1 to 4-10). On a larger scale, waste heat will alter the mineralogy of the host rock and may change the character of the zeolitic units below the potential repository that are likely to be the primary natural barriers to radionuclide migration (Bish 1995, p. 259). For this reason, modeling studies at the drift scale (Buscheck et al. 1996) and site scale (Buscheck and Nitao 1993; Robinson et al. 1996; Pruess et al. 1990) have been conducted to estimate the magnitude of these effects.

The impact of waste heat on the near-surface temperature within the soil zone is the focus of the present study. Since 1990, the Nuclear Waste Technical Review Board (NWTRB) has raised the issue of potential impacts on the aboveground ecosystem from increases in soil temperatures. Both spatial and temporal scales are important in judging the potential significance of increased soil temperature. It is important to understand where areas of higher temperature rise are likely (e.g., drainages, fault lines?). Furthermore, any assessment of the importance must consider the time frame over which temperatures are likely to be elevated (100 yr versus 10,000 yr from the time of emplacement). At more restricted time scales, it is relevant to consider not simply the average temperature rise but also the change to the normal seasonal soil heating and cooling patterns. Growth and productivity of vegetation at Yucca Mountain are largely dependent on precipitation during the winter and spring. However, soil and ambient air temperatures are often too low during much of this period for plant growth until late February and early March. A question of interest is whether the soil-temperature increases will be sufficient to shift the normal growing season to earlier in the year. Although the complex interactions of the ecosystem and subsurface are not explicitly being modeled here, it is expected that the results of the current modeling effort will provide information needed to assess the importance of repository waste heat on the ecosystem.

For the reasons cited above, estimates of the duration, magnitude, and timing of the change in soil temperatures caused by repository waste heat are needed. This study is a first step toward understanding the relevant heat-transfer processes that control the near-surface thermal regime and to place bounds on the expected timing and magnitude of the temperature rise. Two-dimensional, site-scale thermohydrologic calculations will be used to simulate the large-scale thermohydrologic processes that will feed heat to the soil zone. The potential influence of this heat on soil-zone temperatures will then be examined in a series of simplified one-dimensional model calculations. In future efforts, the measured soil-zone temperature variations in response to diurnal and annual temperature variations in the air will be used to calibrate the model, which will tighten the bounds on the possible temperature rise. This study is a precursor to more detailed, three-dimensional simulations with a calibrated model. If it is determined that direct coupling of the site scale and soil zones would be beneficial, this will be done as well.

2. MODELING APPROACH

Current site-scale models of the thermohydrologic behavior in the presence of repository waste heat are typically performed on coarse grids capable of capturing the general features of moisture and heat-flow processes within the unsaturated zone but cannot be used to determine fine-scale temperature and moisture-content gradients. Of relevance in the present study is the representation of the near-surface behavior. The soil zone itself is not explicitly represented in these unsaturated-zone models. Instead, the finite-difference or finite-element grid is initiated at the top of the bedrock in the Tiva Canyon welded (TCw) unit, or whichever other unit is the uppermost in the stratigraphy. Overlying soils, though not explicitly present in the models, exert an impact on the unsaturated-zone flow and transport processes, particularly infiltration rate (Flint et al. 1996, p. 1). The method for incorporating the influence of soil-zone processes on fluid flow has been to rely on near-surface measurements and modeling studies such as those of Flint et al. (1996) to supply maps of deep infiltration rate (the rate of water movement into the fractured bedrock) that accounts for variations in precipitation, evapotranspiration, and runoff. Alternatively, more simplified representations of spatially and/or temporally averaged infiltration rates are used. Thus, current model domains have not been constructed to capture the details of near-surface conditions and cannot be used directly to predict soil-zone temperatures.

Even if the soil zone were explicitly captured as part of the structural model upon which the numerical grid is based, the level of grid resolution typically present in most site-scale models would be insufficient to capture the detailed temperature patterns within the soil zone as a function of diurnal and annual variations in air temperature. Because these measurements will be one of the primary data sets for calibrating the model, a different approach to model development is clearly needed. In the present study, we develop a hybrid modeling approach consisting of a site-scale unsaturated-zone thermohydrologic model to capture the large-scale heat-transfer processes for the purpose of determining the time-varying and spatially nonuniform heat flux supplied to the soil zone. Once this heat flux is known, it is then supplied to a one-dimensional, finely discretized heat-transfer model for the soil zone. In this model, it is much simpler to vary the important parameters of the system, including the thermal properties of the soil, the soil thickness, and the time-varying surface-temperature boundary condition. In this way, we effectively decouple the large-scale thermohydrologic model from the near-surface soil-zone heat-transfer model. The price to pay for this simplification is the added uncertainty associated with decoupling two model domains that are, in fact, coupled. For example, if the repository heat affects the vegetation, and this, in turn, impacts the shallow infiltration source term, then this decoupled model will not have captured the totality of the influence of waste heat. Careful examination of the model results, and further iterations of this study to examine key issues, will be required to assess the validity of the conclusions.

In the following subsections, we describe the model assumptions and model setup for the two submodels in greater detail.

2.1 SITE-SCALE UNSATURATED-ZONE THERMOHYDROLOGIC MODEL

The model domain for the site-scale simulations will be a two-dimensional, East-West cross section at Antler Ridge, used in previous modeling studies to simulate radionuclide transport (Robinson et al. 1995, p. 61; 1996, p. 93) and thermohydrologic behavior (Robinson et al. 1996, p. 93). The relation of this cross section to the ESF and three-dimensional hydrologic model domains is shown in Figure 1, a map of spatially varying infiltration estimated by Flint et al. (1996, Figure 46). This map is used for setting the spatially varying infiltration rate for one of the model cases. Other constant infiltration-rate cases are also considered to capture the uncertainty in this important boundary condition. A depiction of the layered stratigraphy and finite-element grid generated for this cross section is shown in Figure 2. The stratigraphy is captured in detail for the 19 hydrostratigraphic units present in this cross section, and hydrologic properties for the materials are assigned within each unit from values used by Robinson et al. (1995), derived from Wittwer et al. (1995, Table 7), and Loeven (1993, pp. 15–34). The detailed grid resolution near the potential repository is needed to capture the temperature and fluid-saturation profiles near the source of the waste heat. Currently accepted reference-design conditions are assumed for the heat load: inventory of waste totalling 70,000 metric tons uranium (MTU) with an 83 MTU/acre initial heat load and with waste emplaced in drifts that are 22 m apart. At the repository portion of the model (Figure 2d), heat is supplied to individual nodes of the grid along a series of nodes spaced 22 m apart so that, in these calculations, there are roughly four unheated nodes between each node representing an emplacement drift. In the unmodeled direction, the heat load is assumed to be uniform so that the appropriate heat load in the two-dimensional cross section (taken by convention to be 1 m thick) can be applied.

The equivalent-continuum model (ECM) is used to represent the hydrologic properties of a medium consisting of both fractures and intact matrix rock. For the purposes of this study, this approximation is valid because the primary deviations from purely conduction-driven heat transfer are apt to be due to gas-phase transport of latent heat as steam. The ECM approximation does a good job of representing the fracture-dominated permeability of the gas phase in a partially saturated, fractured rock. Its principal deficiencies are in its relatively poor representation of the liquid-phase permeability under unsaturated conditions and the transport of chemical solutes, neither of which are under examination in the present study.

The time-varying heat load issuing from the repository is shown in Figure 3, from data supplied by Tom Buscheck via Bill Glassley, LLNL, on August 7, 1995. The highest heat loads are supplied to the unsaturated zone within the first 100 yr after waste emplacement. Other thermal and hydrologic boundary conditions are required to perform the calculations. At the surface, we assume a variety of temporally invariant infiltration rates, including 1 mm/yr uniform, 4 mm/yr uniform, and the spatially varying infiltration rate shown in Figure 1, which averages 4.8 mm/yr at this cross section. For a detailed modeling study justifying this selection of infiltration rate scenarios, see Viswanathan et al. (1998, pp. 261–262). This range represents the current range of estimates based on surface infiltration and environmental isotopes. The range is retained in this study to examine the impact of this uncertainty on the model results. The fluid-flow boundary condition at the bottom of the model domain is a fluid saturation of one to represent the water table.

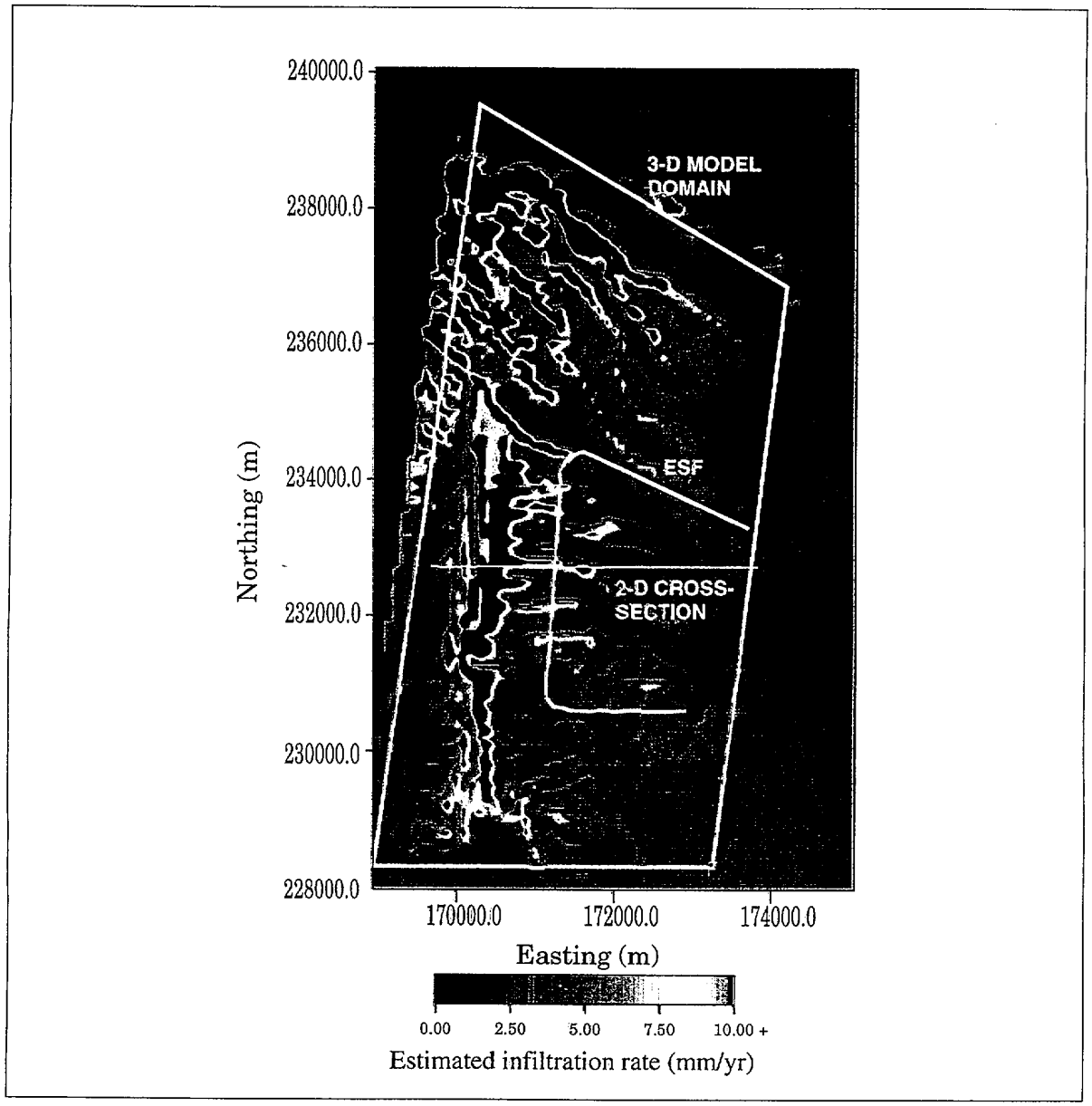

Figure 1. Map of Spatially Varying Infiltration Rate (based on Flint et al. 1996). Also shown is the outline of the 3-D model domain used in Robinson et al. (1995; 1996) along with the location of the 2-D cross section used in the present study. (DTN: LABR150191DN99.001)

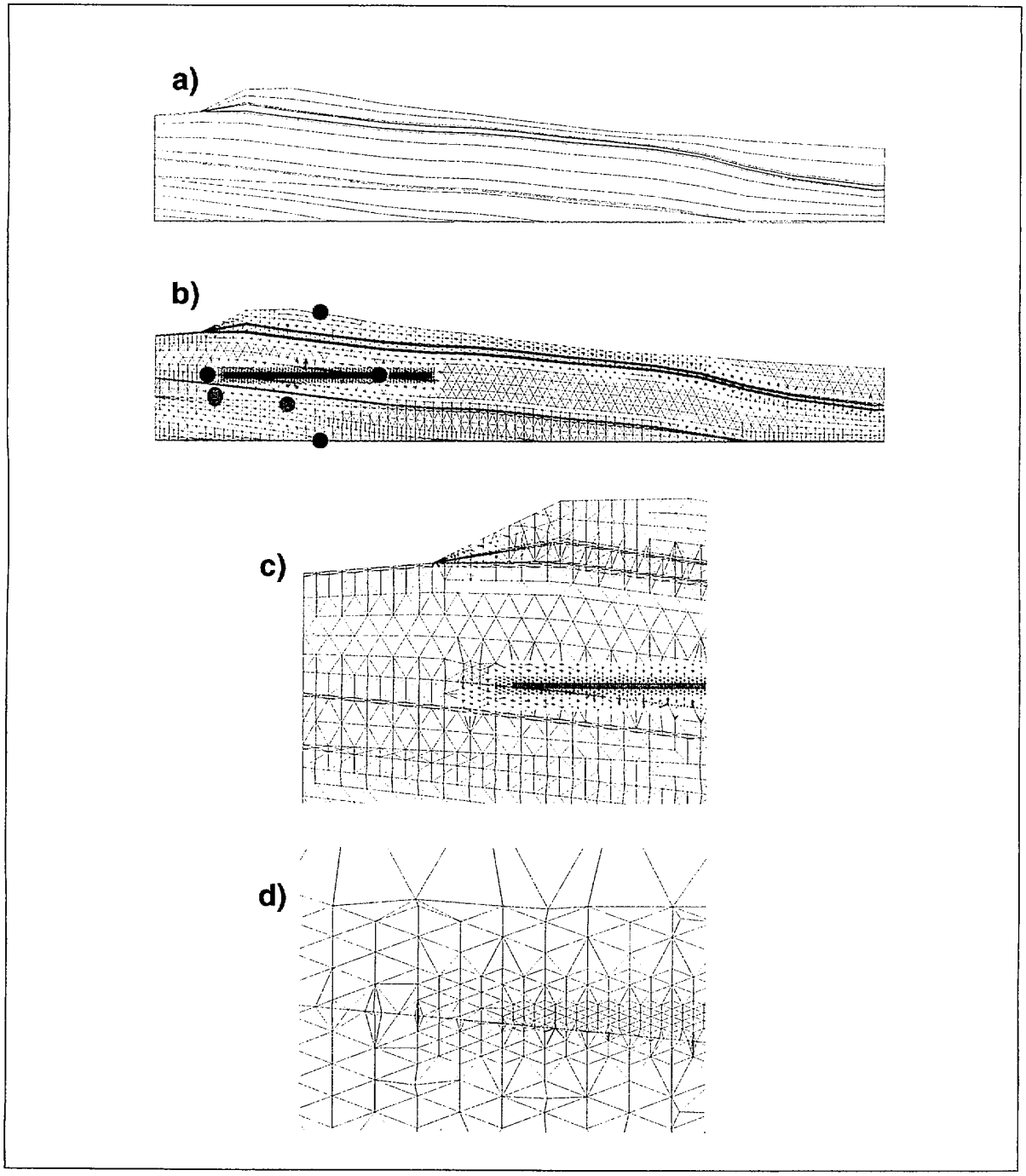

Figure 2. Two-dimensional Antler Ridge Model Domain.
The figure shows a) the geometry of the stratigraphic layers; b) the computational grid; c) a close-up view of the western area of the grid; and d) a close-up of the grid at the western edge of the repository region. The colored dots in b) represent locations used for reporting results: red—repository; blue—surface or water table; green—Calico Hills unit. (DTN: LABR150191DN99.001)

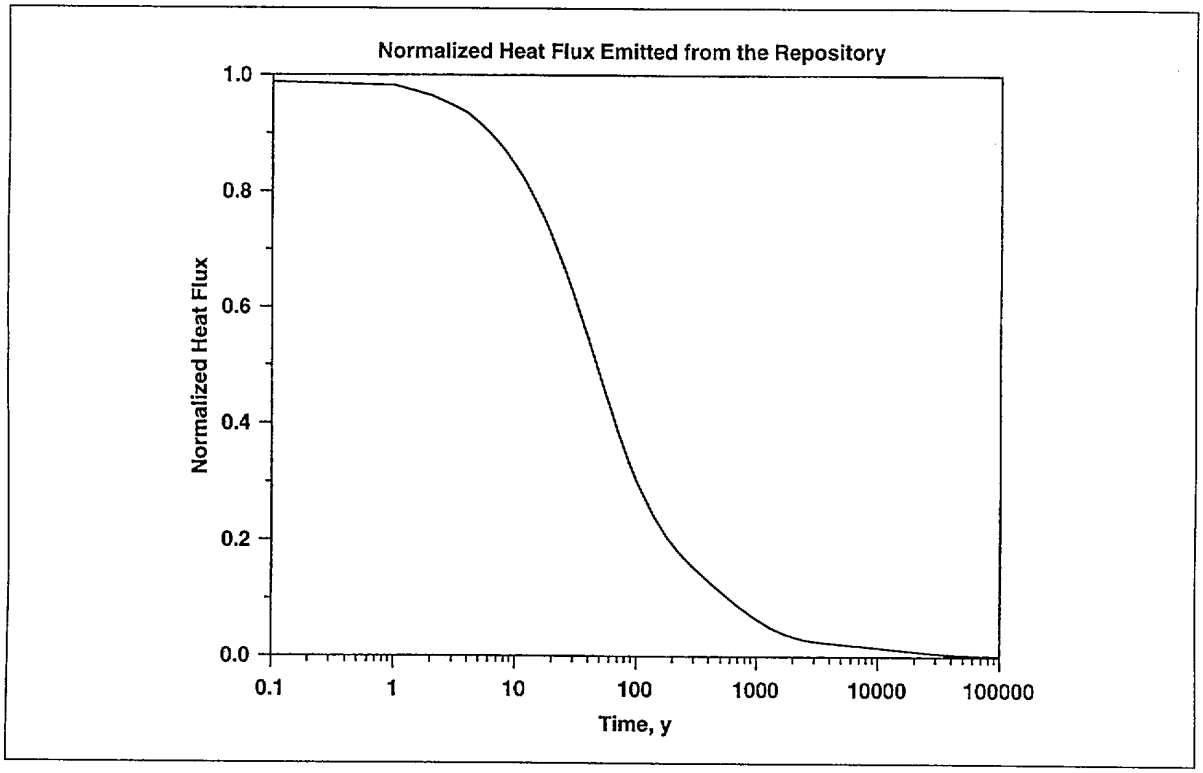

Figure 3. Normalized Heat Flux Due to Radioactive Decay Heat.
The figure is a plot of the normalized heat flux versus time due to radiaoactive decay waste heat from the potential repository (data supplied by Tom Buscheck via Bill Glassley, LLNL, on August 7, 1995). (DTN: LABR150191DN99.001)

The thermal boundary conditions at the top and bottom of the model are potentially more important to the present study and, thus, will now be presented in greater detail. The finite-element heat- and mass-transfer numerical code, FEHM, used to perform the calculations, has an option for a flux-based boundary condition to set thermal boundary conditions that take the form

$$Q_b = \Omega(T - T_b), \tag{1}$$

where Q_b is the rate of heat removal from a node (in MW), T is temperature at the boundary node, T_b is the temperature outside of the model domain at which the heat exchange is taking place, and Ω is a scaling parameter. If we consider that the boundary condition is meant to represent heat transfer at the interface of the model domain and the exterior of the model (e.g., within the atmosphere for the ground surface), Ω is equivalent to hA_n, the product of the heat transfer coefficient times the area normal to the surface. Setting Ω to a high enough value allows the simulation to be performed as a prescribed-temperature boundary condition (T_b) while retaining the capability of recording the heat flux entering or leaving at the node. This method is used for the ground surface to simulate the condition of efficient heat transfer, such that the surface temperature equals the assumed air temperature. This air temperature (and air pressure)

are assigned elevation-dependent, time-invariant values based on a method developed by Ross et al. (1992) designed to capture elevation dependence of air properties. For the Ω parameter chosen for the surface boundary condition, the temperature T along the upper surface is held at the value of T_b to at least six decimal places, and the code output of Q_b along the surface is recorded at the surface. For the bottom boundary (the water table), two end-member cases are considered:

- efficient heat transfer (large Ω), representing the case of heat transfer by convection of flowing saturated-zone fluid, and
- conduction-limited heat transfer, as approximated with an appropriately low value of Ω.

Strictly speaking, the method reflected in Eq. 1 cannot exactly duplicate the process of thermal conduction within the saturated zone, but a reasonable approximation can be developed from consideration of the thermal-diffusion length scale. First, note that one-dimensional thermal conduction is governed by

$$Q_b = kA_n \frac{\partial T}{\partial z}, \tag{2}$$

where k is the thermal conductivity within the saturated zone and z is the downward direction. To approximate the mechanism of thermal conduction within the saturated zone, the scaling factor becomes

$$\Omega = \frac{kA_n}{\Delta z}, \tag{3}$$

where Δz is a characteristic distance for thermal diffusion, assigned using an order-of-magnitude estimate for thermal diffusion:

$$\Delta z \cong \sqrt{\alpha t_d}, \tag{4}$$

where the thermal diffusivity α is given by $\alpha = k/(\rho c_p)$, where ρ is the rock density and c_p is the rock heat capacity. The time scale for thermal diffusion t_d within the saturated zone is required to set an appropriate value for Δz and, hence, Ω. This time is roughly the time period over which significant heat is being transmitted into the saturated zone due to radioactive decay. We take 10,000 yr as an appropriate value for this time. Once heat reaches the water table, the temperature at the water table will then begin to rise in a manner similar to what would be obtained if the unsaturated and saturated zones were simultaneously modeled but without the additional computational overhead of including the saturated zone.

2.2 ONE-DIMENSIONAL SOIL-ZONE MODEL

Within the soil zone, we assume that a thermal-conduction model captures the essential physics of the heat-transfer process. We, therefore, ignore the influence of evapotranspirative (ET) processes on the energy balance. Thermal conduction is the starting point of most developments of soil-zone thermal analyses (e.g., Hillel 1980a and b; Marshall and Holmes 1979; Hillel 1982). In FEHM, there is a provision for simulating pure heat conduction without fluid flow. This model assumption is employed in the present study to provide a first estimate of the potential rise in soil temperature due to repository waste heat. The one-dimensional finite-element grid used to simulate soil-zone heat transfer consists of a column of elements extending to a depth of 50 m, well into the bedrock at most locations at Yucca Mountain. Extending the model to depths of 50 m ensures that any perturbations due to diurnal and seasonal temperature variations are almost completely damped at this depth. This condition is required so that the bottom boundary can be set using a heat-flux condition, either the ambient geothermal heat flux or the repository-enhanced heat flux predicted from the site-scale model.

The grid discretization was set to capture the thermal response at a variety of time scales. The first meter of depth consists of nodes spaced 1 cm apart to capture temperature gradients due to diurnal effects. From 1-m to 5-m depth, spacings are 5 cm, a coarser discretization but nonetheless adequate to capture deeper-penetrating seasonal variations in temperature. The final 45 m of the model are represented using 20 nodes of increasing spacings as a function of depth to provide a coarse representation of the bedrock. Thermal gradients at depths greater than about 5 m are likely to be small compared to those caused by diurnal or seasonal surface-air-temperature variations, and thus, the grid need not be fine to capture the heat-transfer processes in the bedrock. If desired, soil zones of different thickness can be studied with this grid, because the assignment of thermal properties can be made from node to node at runtime, independent of the numerical grid.

Using a pure-conduction model requires that the thermal properties of the medium be assigned to represent a partially saturated soil. For thermal conduction, the entire transient heat-transfer system is controlled by the thermal diffusivity α, given by $\alpha = k/(\rho c_p)$. The property values used for this modeling are either measured values (bulk density) or estimated values based on soil moisture content and porosity. Maps of soil characteristics at or near the potential repository footprint published by Flint et al. (1996, Figure 14) show that the predominant soil unit within the model domain is termed Lithic Haplocambids (Model Unit 5 of the Flint et al. report). It comprises 47% of the surface soils in the entire study area and, from inspection of Figure 14 of the Flint et al. (1996) report, a much larger percentage of the soil coverage directly above the potential repository. Therefore, we assume that the properties measured for their Model Unit 5 are appropriate for the present study. The bulk density ρ for this soil is found to be 1.69 g/cm^3 with a porosity of 0.33 (Flint et al. 1996, Table 4).

For heat capacity, a weighted average of the heat capacities of the individual constituents of the soil is adequate (e.g., Marshall and Holmes 1979), which requires an estimate of the water content of the soil. The volumetric water content will vary strongly in space and time due to spatially and temporally varying pulses of water infiltration after precipitation events. To begin to examine the

heat-transfer process, we take the simplifying assumption that the water content is constant throughout the soil and vary its value to examine the impact on heat transfer. For the nominal case considered here, we assume a water content of 17%, the equivalent of 50% saturation in a soil with 0.33 porosity. This value is estimated from inspection of figures depicting the measured volumetric water content of soils at various neutron boreholes at Yucca Mountain by Flint et al. (1996, Figures 31 and 32). The value is then varied in a sensitivity analysis from 5% to 33% (fully saturated) to capture the variability observed at the site. The low value represents a value during dry periods and at locations where ET effects are strong, resulting in efficient desiccation of the soil, whereas 33% is a value that might be encountered closer in time to an infiltration event or during a possible wetter future climate. Corresponding values for the heat capacity are shown in Table 1.

Thermal conductivity varies even more strongly with water content than does heat capacity. The process is dominated by not simply the relative amounts of solids, water, and air but also on the details of the interconnected network of thermally conducting solids and water, which is interspersed with air, a poor heat conductor. There are theories for estimating the thermal conductivity of a partially saturated soil (e.g., Hillel 1980a). The thermal conductivity of the soils at Yucca Mountain are apt to be a strong function of the time relative to the infrequent rainfall events that occur at the site. In between these events, the uppermost meter of soil is likely to dry very efficiently, especially in the summer, which could reduce the thermal conductivity markedly. As a starting point, we assume that the range is covered by assuming the soils at Yucca Mountain span the measured range for a sandy soil as a function of water content as reported by Hillel (1980a). The dry, nominal, and wet thermal conductivities listed in Table 1 correspond to water-content values for the soil reported in this reference of 0, 0.2, and 0.4, respectively. The resulting values for thermal diffusivity α given in Table 1 show that the value goes through a maximum at a partially saturated condition at which the thermal conductivity no longer continues to increase significantly with increasing water content, whereas the heat capacity continues to rise. In a subsequent section, we analyze the measured thermal response of the soil to diurnal changes in air temperature as a method for calibrating the model. Finally, the bedrock is given thermal properties of the welded Tiva Canyon tuff given in CRWMS M&O (1995, p. 4–19).

Table 1. Soil Thermal Properties Used in Model Calculations. (DTN: LABR150191DN99.001)

Soil Type	Moisture Content	Density ρ (kg/m^3)	Heat Capacity c_p (J/kg-K)	Thermal Conductivity k (W/m-K)	Thermal Diffusivity α (10^{-7} m^2/s)
Dry	0	1700	500	0.3	3.5
Nominal	0.17	1900	1220	1.8	7.8
Wet	0.33	2000	1890	2.2	5.8

Methods for applying the thermal boundary conditions are similar to those discussed for the site-scale modeling above. For the bottom boundary, the heat flux is input directly. Its value is either a value typical of the ambient heat flux at Yucca Mountain (35 mW/m^2, after Sass et al. 1988) or is obtained from site-scale model results for the heat flux at the surface due to potential repository waste heat. The surface boundary condition is handled assuming a heat-transfer-coefficient model (Eq. 1) with an estimate of the heat-transfer coefficient meant to provide an upper bound on the possible rise in surface and near-surface soil temperatures. For this, a minimum estimate of the heat-transfer coefficient is needed. Ignoring radiative heat transfer, the effect of ET on the energy balance, and forced-air convection due to air circulation along the surface of Yucca Mountain, the minimum heat-transfer coefficient possible is due to natural convection of air next to a heated surface. Taking a minimum heat-transfer coefficient of about 3 W/m^2-K for natural convection of air (Bennett and Myers 1974), the end-member of least-efficient heat transfer to the atmosphere will be obtained. If even this value results in effective heat transfer from the soil surface to the atmosphere (i.e., low ΔT between the soil and atmosphere) then more detailed estimates of the heat-transfer mechanisms coupling the soil and atmosphere are unnecessary for estimating potential increases in soil temperature.

3. SITE-SCALE MODEL RESULTS

In this section, we report results of the site-scale unsaturated-zone thermohydrologic model. Although the present study is examining the impact of repository heat on soil temperatures, we begin with a more general discussion of the predicted behavior in the unsaturated zone. Figure 4 shows the predicted fluid-saturation response of the system at a uniform 1-mm/yr infiltration rate and illustrates the redistribution of fluid due to heat-up near the emplacement drifts. Over a period of roughly 10,000 yr, dryout and rewetting occurs near the emplacement drifts. A two-phase, countercurrent flow zone develops above the potential repository with buoyant and pressure-gradient-driven vapor movement in the upward direction counterbalanced by downward fluid percolation, the primary source of which is condensed steam. The resulting heat-transfer mechanism, called a heat pipe, is much more efficient than thermal conduction alone and results in an extended two-phase region of enhanced heat transfer at about 1 atm and 100°C. This effect is seen most easily in the temperature fields of Figure 5. When the heat from the repository region is insufficient to maintain the two-phase zone, the zone collapses, and fluid reenters the repository region. The extent of the two-phase region is controlled by the nature of the fracture system, because transport of latent heat (as steam) increases with increased fracture permeability. In these simulations, the fracture permeabilities in the PTn are low enough that the upward advance of the heat-pipe region is arrested at the base of the PTn, and conduction is the primary mode of heat transfer to the surface. The rewetting of the repository and rebounding of the system to its ambient conditions occurs within 10,000 yr of waste emplacement. Its nonuniform character is due to the various hydrologic parameters in the subunits of the TSw near the repository.

The temperature and fluid saturation near the emplacement drifts controls the hydrologic and gas-phase moisture conditions that, in turn, control the degradation of the protective waste-package containers and the dissolution of the solid radioactive waste. Figure 6 shows the predicted fluid-saturation distribution near the emplacement drifts at 100 and 1,000 yr after emplacement. Complete dryout of the rock near each drift is predicted, and the duration of complete dryout conditions depends on position within the repository. Closer to the middle of the repository, dryout regions associated with the individual drifts are predicted to merge, forming a continuous region of dry rock through which fluid cannot percolate. In contrast, an "edge effect" is predicted for drifts at either end of the repository where enhanced downward percolation and lateral cooling effects inhibit dryout zones from coalescing.

Waste-package degradation and waste-form dissolution are dependent on the time history of temperature, fluid saturation, and relative humidity in the rock near the emplacement drifts. Figure 7 shows the predicted saturation versus time in the rock near two emplacement drifts (one closer to the middle of the repository and one near the edge) for the 4-mm/yr-infiltration-rate scenario (other infiltration rates yield similar results), and Figure 8 is the time history of temperature at these locations and illustrates the relatively minor impact of infiltration rate as well. After an initial warm-up period lasting less than one year, a boiling period lasting on the order of 10 yr is needed to dry the rock near the drift, after which time the rock heats to values greater than the boiling temperature for a substantial period. During this time, the relative humidity near the waste packages can decrease to favorably low values (Figure 9). The period of

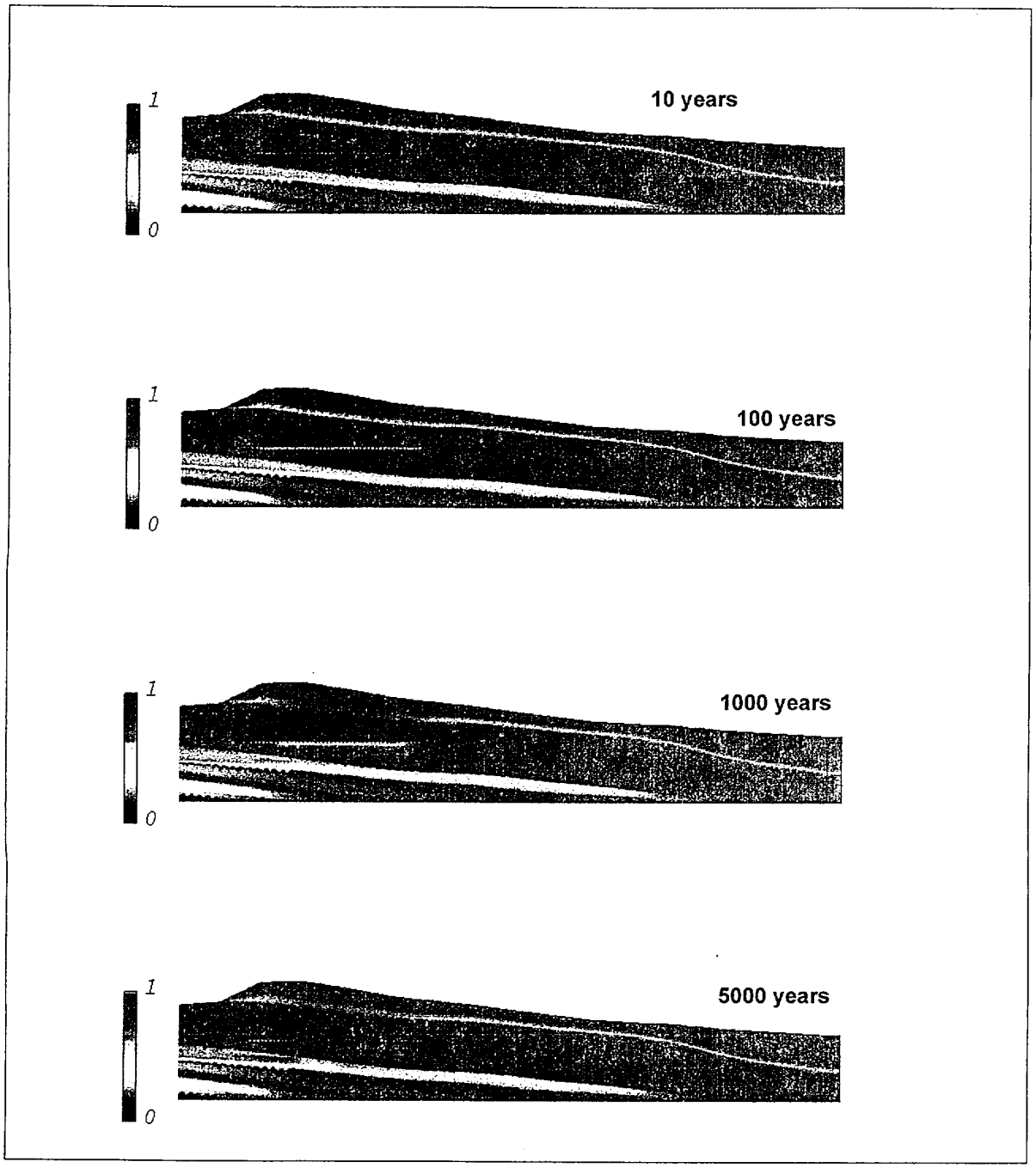

Figure 4. Unsaturated-zone Fluid Saturation.
The figure shows unsaturated-zone fluid saturation at various times after emplacement of the waste. (DTN: LABR150191DN99.001)

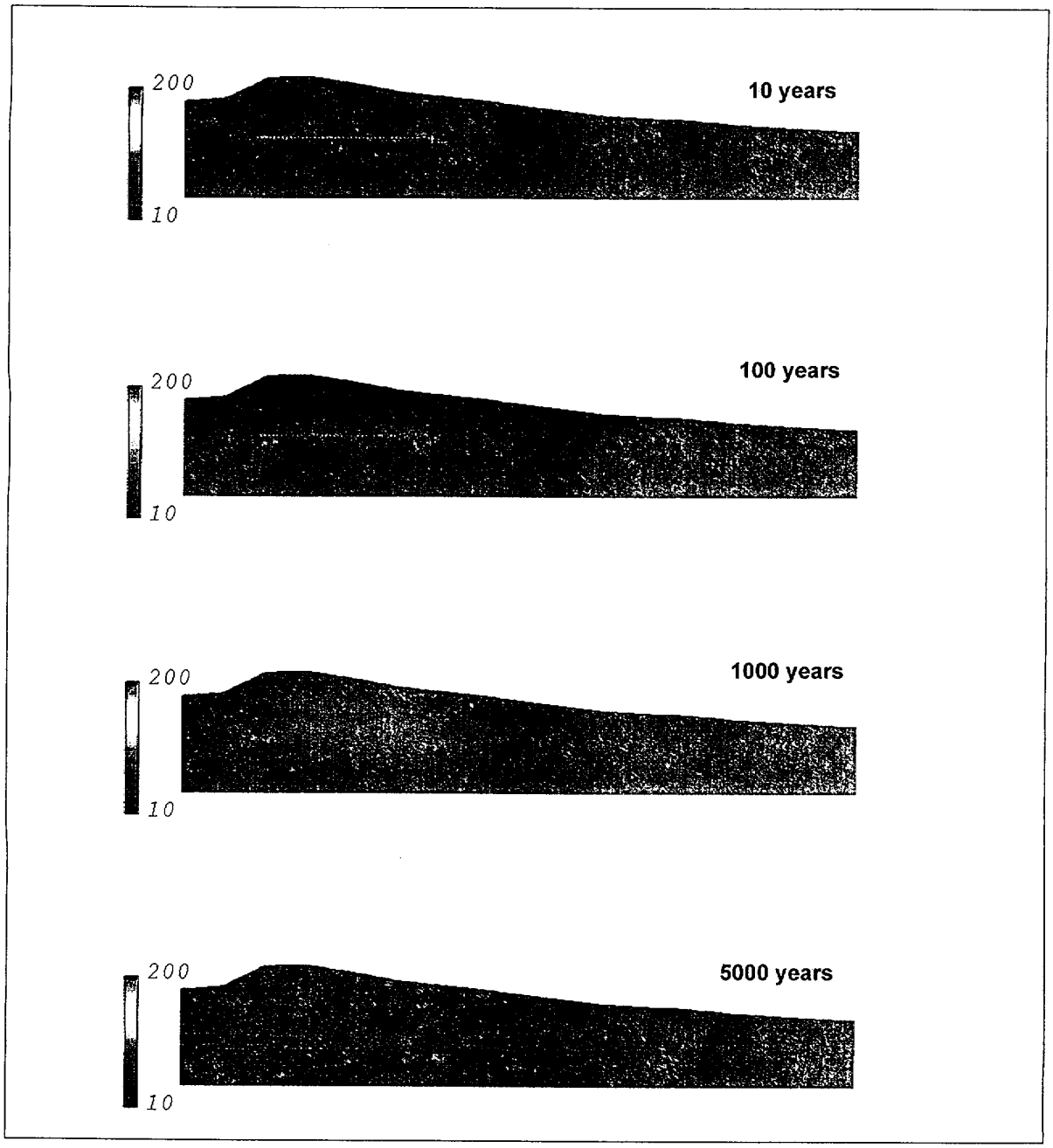

Figure 5. Unsaturated-zone Temperature.
The figure shows unsaturated-zone temperature (°C) at various times after emplacement of the waste. (DTN: LABR150191DN99.001)

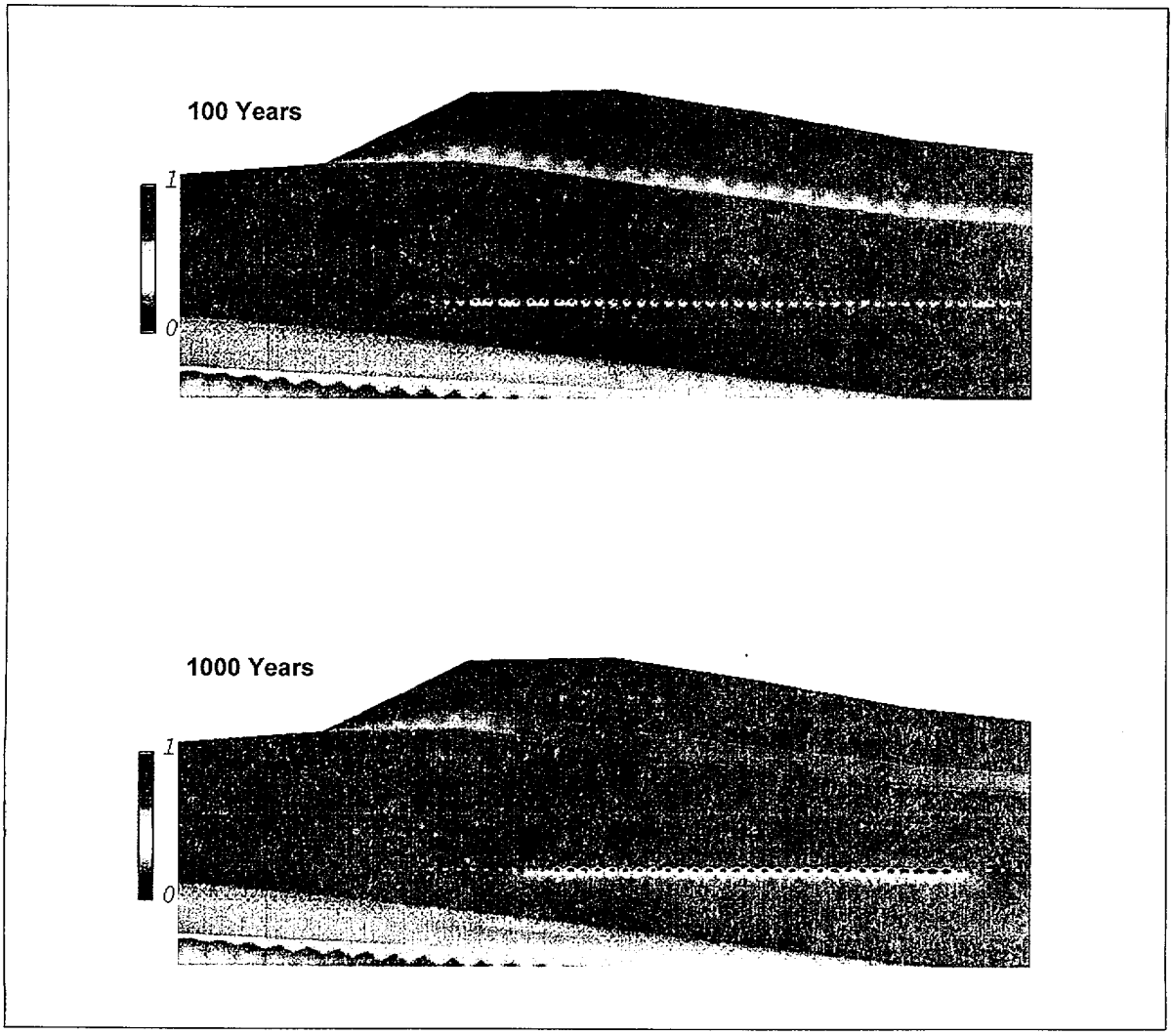

Figure 6. Fluid-saturation Distribution Near Potential Repository.
The figure gives a closeup view of the distribution of fluid saturation near the potential repository.
(DTN: LABR150191DN99.001)

complete dryout at a given infiltration rate depends most critically on the position of the drift within the repository. For example, for the variable-infiltration scenario, the onset of rewetting is predicted to occur within the first 100 yr near the repository edge and between 500 and 1000 yr for an inner drift. The infiltration rate itself plays a smaller role in the predicted onset of rewetting and the large-scale thermal response with relatively small differences in predicted rewetting time and temperature-time history at various locations. Temperatures near the emplacement drift vary most strongly with position in the repository, with maximum values approaching 190°C for inner drifts and only 140 to 170°C for edge drifts. Even though the

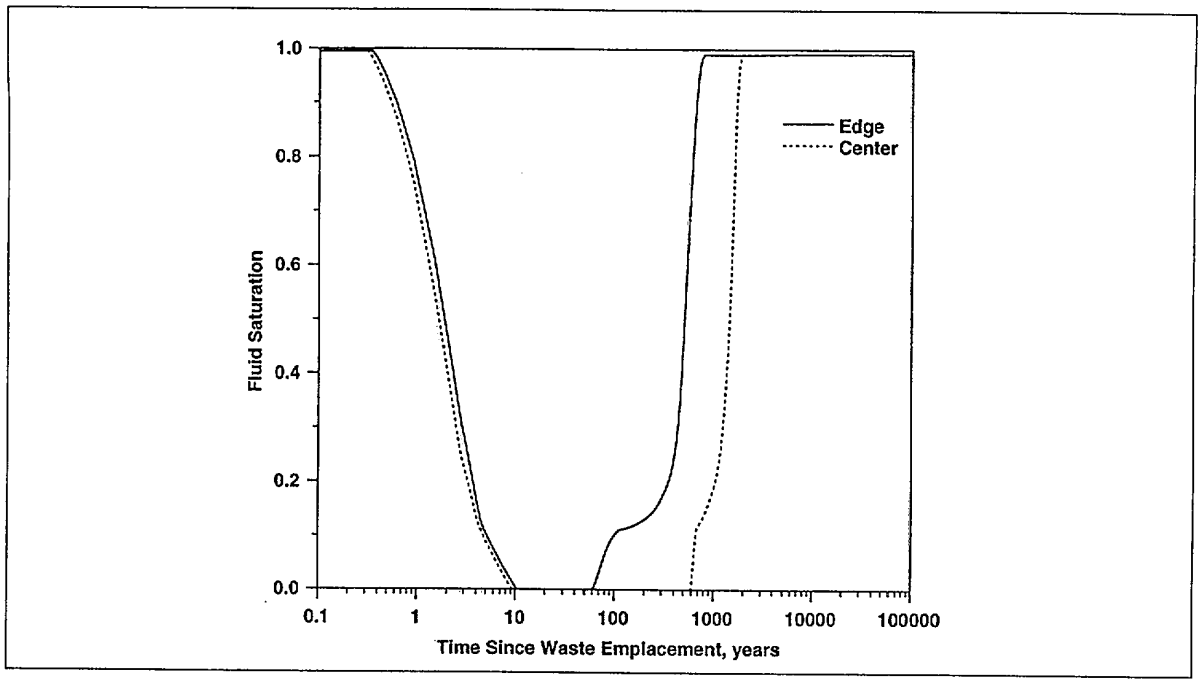

Figure 7. Saturation in Rock Near Two Emplacement Drifts.
The figure shows saturation versus time in the rock near two selected emplacement drifts (locations given in Figure 2) for a 4-mm/yr-infiltration-rate scenario. (DTN: LABR150191DN99.001)

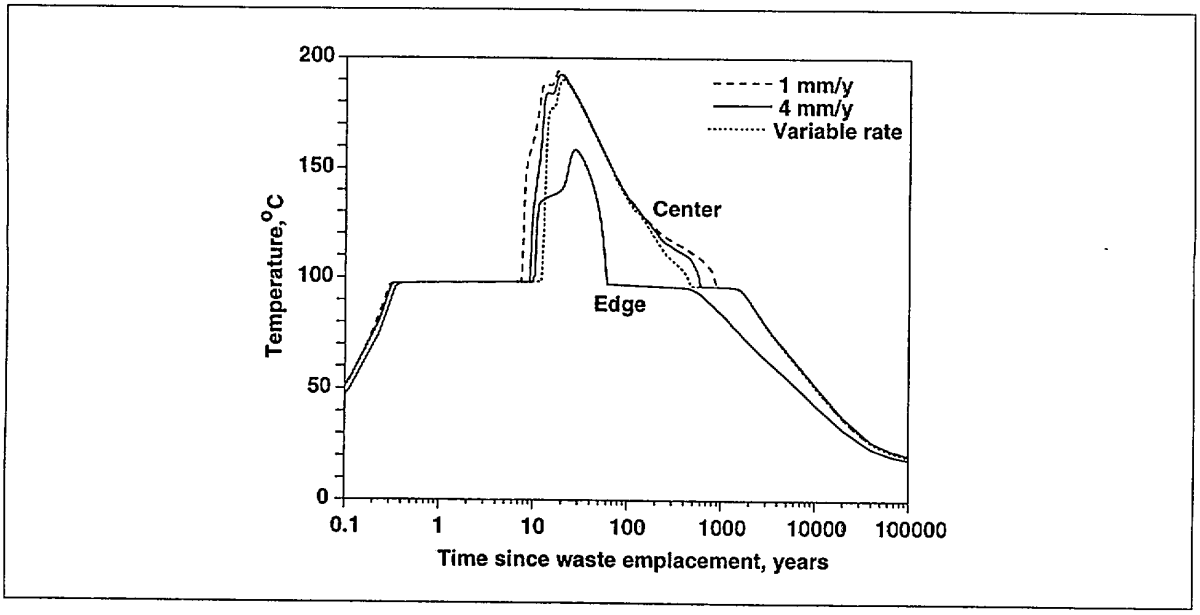

Figure 8. Temperature in Rock Near Two Emplacement Drifts.
The figure shows termperature versus time in the rock near two selected emplacement drifts (locations given in Figure 2) for various infiltration-rate scenarios. (DTN: LABR150191DN99.001)

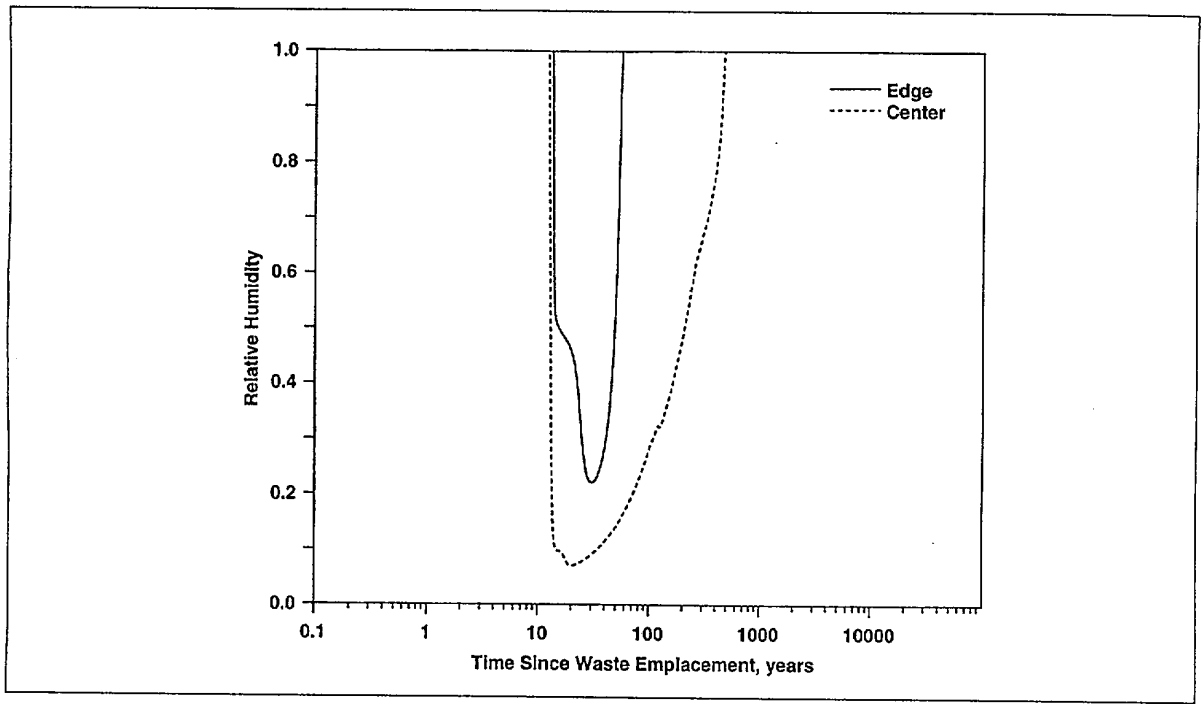

Figure 9. Relative Humidity in Rock Near Two Emplacement Drifts.
The figure shows relative humidity versus time in the rock near two selected emplacement drifts (locations illustrated in Fig. 2) for variable infiltration rate scenario. (DTN: LABR150191DN99.001)

infiltration rate is thought to vary considerably across the model domain (Figure 1), the influence on the model results, for the purpose of predicting the rise in soil temperatures, is minor.

The necessity of adequate grid resolution near the potential repository is illustrated in Figure 10, a plot of predicted temperature versus time assuming that the heat load associated with the waste heat is uniformly distributed within a 5-m-thick rectangular region extending the length of the repository. Temperatures at the same locations as in the distributed-heat cases presented earlier now are predicted to rarely or never exceed the boiling temperature, as the rock fails to fully desaturate. It is necessary to use a finely resolved grid in the vertical and horizontal directions to capture the details of fluid saturation, temperature, and relative humidity near the emplacement drifts. If the modeling objective requires accuracy near the emplacement drifts, as when predicting canister lifetime or radionuclide source terms, then grid resolution is needed, especially in the horizontal direction so that the detailed fluid and thermal patterns at and between drifts can be resolved.

Another important impact of radioactive waste heat on system performance is the extent of temperature rise in the zeolitic rocks below the potential repository. High temperature could result in dehydration or altering of the zeolites of the Calico Hills and underlying zeolitized units, thereby changing the hydrologic and transport properties. Even in the absence of alteration, sorption coefficients and chemical speciation are usually a function of temperature, requiring an

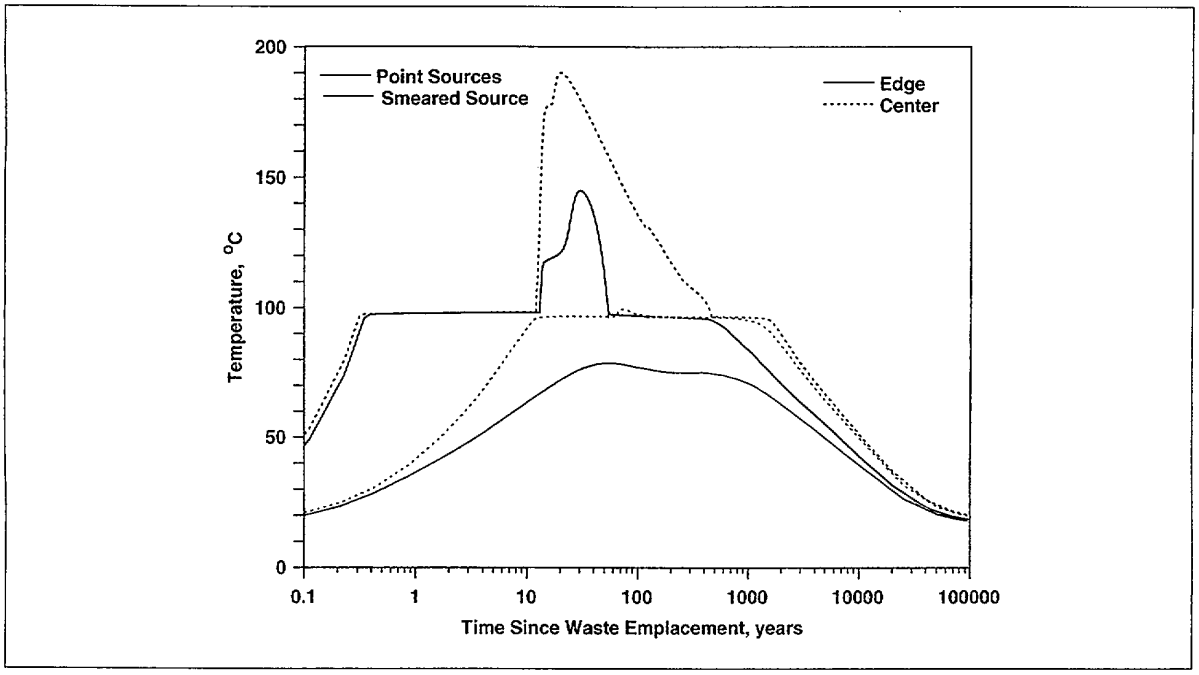

Figure 10. Temperature in Rock Within the Repository.
The figure shows temperature versus time in the rock at two locations within the repository region assuming a "smeared" heat source and a variable infiltration scenario. (DTN: LABR150191DN99.001)

estimate of the magnitude and duration of the temperature rise. Figure 11 shows the predicted temperature-time histories of the positions in the Calico Hills unit representing the top of the zeolitic horizon (positions where the temperatures are recorded as shown in Figure 2b). Examining the curves labelled "isothermal water table," we note that the greater temperature rise occurs for the position that is closer to the middle of the repository heat source, despite the fact that the top of the zeolites is actually 25 m farther from the heat source than for the position below the edge of the repository. The other comparison illustrated in the figure is the impact of the heat-transfer boundary condition at the water table. The conduction-limited model is more insulating than the isothermal condition, resulting in a predicted rise in rock temperature at the water table (the blue curve in Figure 11) of roughly 25°C that subsequently rebounds to the ambient value. This effect, in turn, results in a higher predicted temperature rise in all units between the water table and the repository horizon, including the zeolitic rocks. For example, for the zeolites at the centrally located position, the predicted maximum rise in temperature is from 20°C to 70°C for the isothermal boundary, compared to a rise to 79°C for the conduction-limited case. Infiltration rate has a very minor impact on the predicted temperature rise. The timing of the temperature rise and fall are roughly the same regardless of infiltration rate or water-table boundary condition: for example, the variable infiltration rate exhibits a rise in temperature beginning at 125 yr (5% of the overall rise occurs within 125 yr), goes through a maximum at about 2500 yr, and has returned to within 5% of its original value at 95,000 yr. Finally, the figure shows that the "smeared"

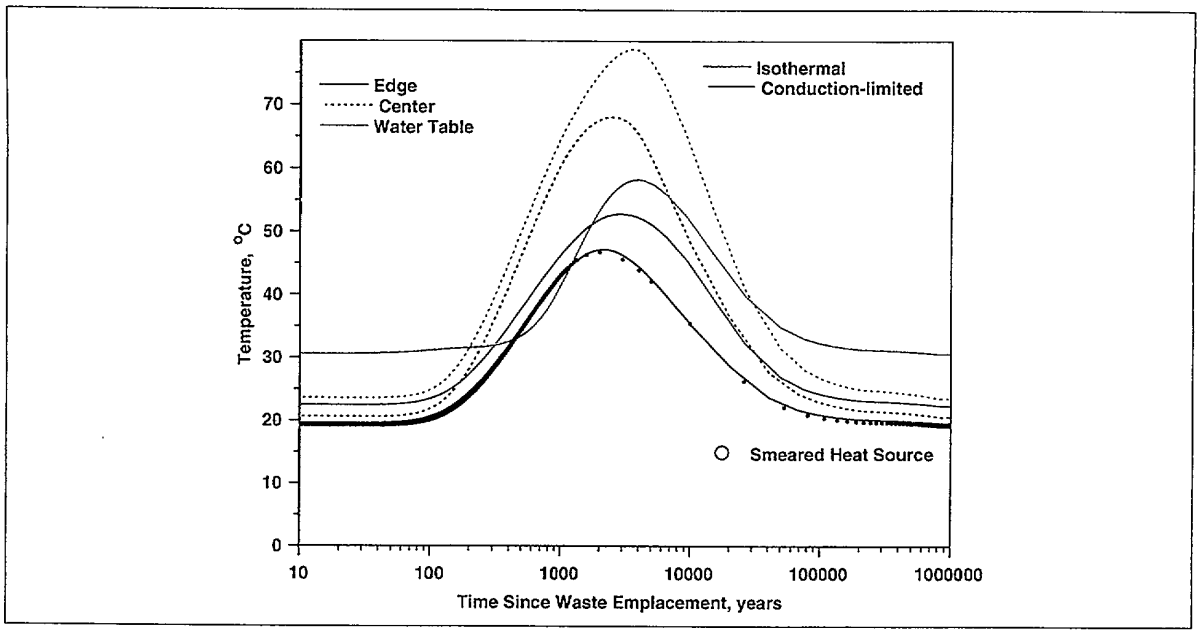

Figure 11. Temperature at the Top of the Calico Hills Unit.
The figure shows temperature versus time at the top of the zeolitic Calico Hills unit (locations given in Figure 2) for the isothermal and conduction-limited water-table boundary conditions. Also shown is the predicted temperature at the water table directly below the heated zone (blue curve) and the results for a smeared heat source (symbols). (DTN: LABR150191DN99.001)

repository heat source yields a virtually identical prediction of temperature rise in the zeolites, illustrating the fact that if predictions are required at a significant distance from the drifts, then a smeared heat source can be used for the boundary condition. Because there is no reason in the present study to resort to the smeared source, the calculations are performed using the point sources of heat to represent heat emanating from each drift.

The predicted heat flux at the surface and its variability with time, infiltration rate, and boundary conditions is required to set appropriate boundary conditions for the one-dimensional soil-zone analyses presented in the next section. Figure 12 shows the spatial distribution of heat flux at 1,000 yr after waste emplacement assuming the isothermal water-table boundary condition. As expected, the heat flux is highest at locations near the center of the surface projection of the repository zone and taper off near the edges. Surface heat-flux values are unchanged from their pre-emplacement values at a distance of roughly 500 m from the edge of the repository. The slight offset of the maximum from the center of the repository is due to a topographic effect. Specifically, the distance from the repository to the surface is closer at positions somewhat to the west of the center of the repository. To display the time variation of heat flux, we select a position where the heat flux at any time is highest. Figure 13 shows the heat flux at this location for the various infiltration-rate scenarios. Infiltration rates play almost no role in the predicted heat flux at the surface because the rise in heat flux overwhelms any ability of the infiltrating fluid to convect the heat away before it reaches the surface.

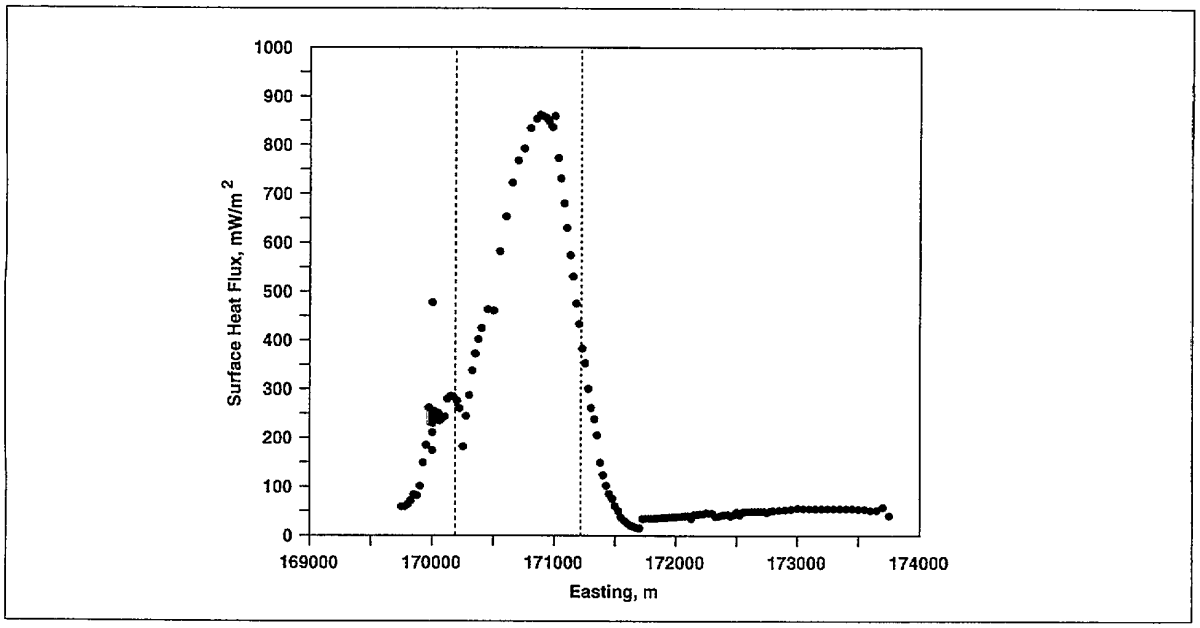

Figure 12. Spatial Variation of Heat Flux at the Surface After 1000 Years.
The figure shows the spatial variation of heat flux at the surface 1000 yr after waste emplacement. The dotted lines indicate the extent of the potential repository projected onto the surface. (DTN: LABR150191DN99.001)

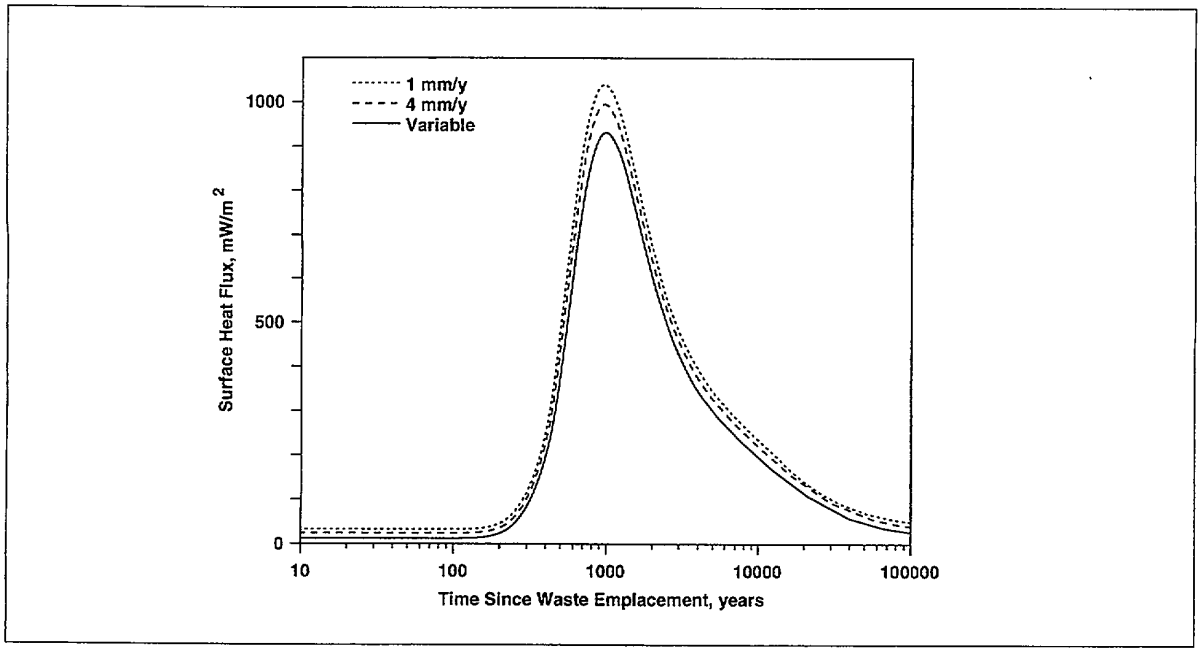

Figure 13. Heat Flux Above Repository for Various Infiltration Rates.
The figure shows the heat flux versus time directly above the potential repository for various infiltration rates. (DTN: LABR150191DN99.001)

The effect of the heat-transfer boundary condition at the water table is shown in Figure 14. Because the temperature rise at the water table does not occur until after roughly 1,000 yr (Figure 11), there is virtually no impact on the heat flux at the surface due to changes in the water-table boundary condition before this time. By the time the water-table boundary condition does affect the surface heat flux, the effect is very small and can safely be ignored. The greatest impact of the water-table boundary condition on the results at the surface occurs at about 10,000 yr, in this case, after the surface heat flux has begun to decline from its maximum.

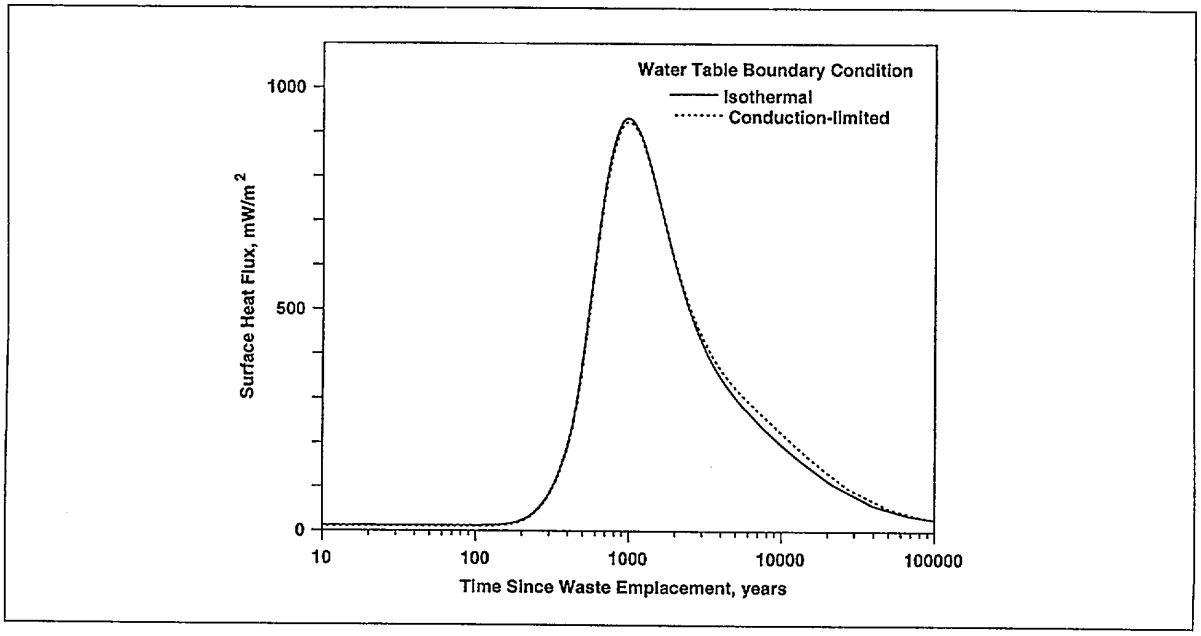

Figure 14. Heat Flux Above Repository for Two Heat-transfer Boundary Conditions. The figure shows heat flux versus time directly above the potential repository for the two water-table heat-transfer boundary conditions. (DTN: LABR150191DN99.001)

The computational burden of performing a series of three-dimensional, thermohydrologic simulations precludes carrying out all of the analyses in three dimensions. Of course, the actual heat- and mass-transfer system is three-dimensional, so it is necessary to assess the validity of the two-dimensional assumption used in the analyses discussed so far. In the present study, this assessment is accomplished in two steps. First, we examine the error associated with assuming that thermal conduction dominates the heat-transfer system by comparing two-dimensional model results with and without the liquid- and gas-phase transport. We then use three-dimensional, "conduction-only" simulations to efficiently examine the influence of the third dimension. The grid used in the three-dimensional simulations was developed in Robinson et al. (1997, p. 3–17) and consists of 71,781 nodes and 414,313 tetrahedral elements.

First, we compare the two curves in Figure 15 that represent the two-dimensional runs. The full thermohydrologic simulation results in a higher peak heat flux at the surface than the conduction-only solution. The heat-pipe effect transmits heat preferentially upward, thereby resulting in a

greater heat loss through the soil layer and to the atmosphere. Therefore, if the goal is to bound the potential increase in soil temperatures, then the full thermohydrologic solution should be used. Because we need to also examine three-dimensional effects using the conduction-only assumption, we must consider the roughly factor-of-two underestimation of the maximum heat flux that results from this simplification. Other aspects of the heat-flux curve, such as the timing and duration of the increase in heat flux, are approximately captured with the conduction-only model.

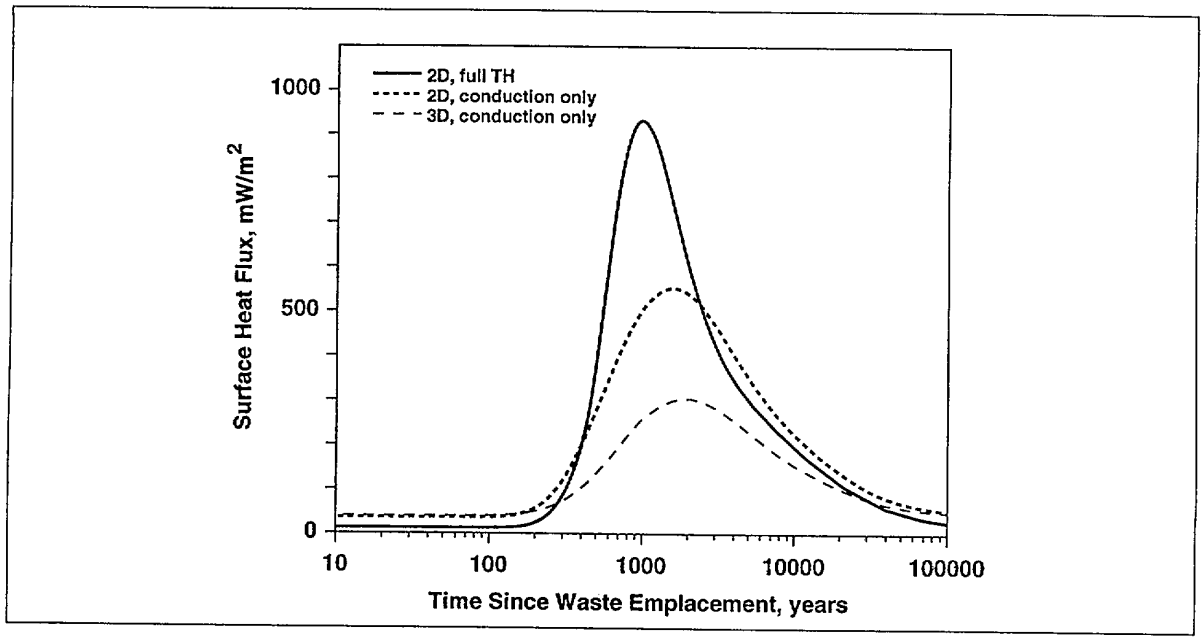

Figure 15. Heat Flux Above Water Table (2-D Full Thermohydrologic, 2-D Heat Conduction Only, and 3-D Heat Conduction Only).

The figure shows the heat flux versus time directly above the water table for various heat-transfer assumptions: 2-D full thermohydrologic simulation, 2-D heat-conduction-only solution, and 3D heat-conduction-only solution. (DTN: LABR150191DN99.001)

We now compare the two- and three-dimensional conduction solutions in Figure 15. The results show that the two-dimensional approximation overestimates the maximum heat flux at the surface. In a three-dimensional system, heat spreads laterally from the heat source in all directions. This effect is illustrated in Figure 16, a map of simulated surface heat flux after 2000 yr, roughly the time of maximum heat flux at the surface. The areal extent of the perturbation from ambient conditions is significantly larger than the potential repository footprint projected to the surface. In two-dimensions, this lateral spreading only occurs in the Easting direction. This fact results in an overestimate of the heat flux directly above the potential repository. Therefore, we have two counteracting errors that need to be considered when carrying out the site-scale simulations. The two-dimensional assumption yields higher predicted heat-flux values than the full three-dimensional solution, but the conduction-limited solution results in an underprediction

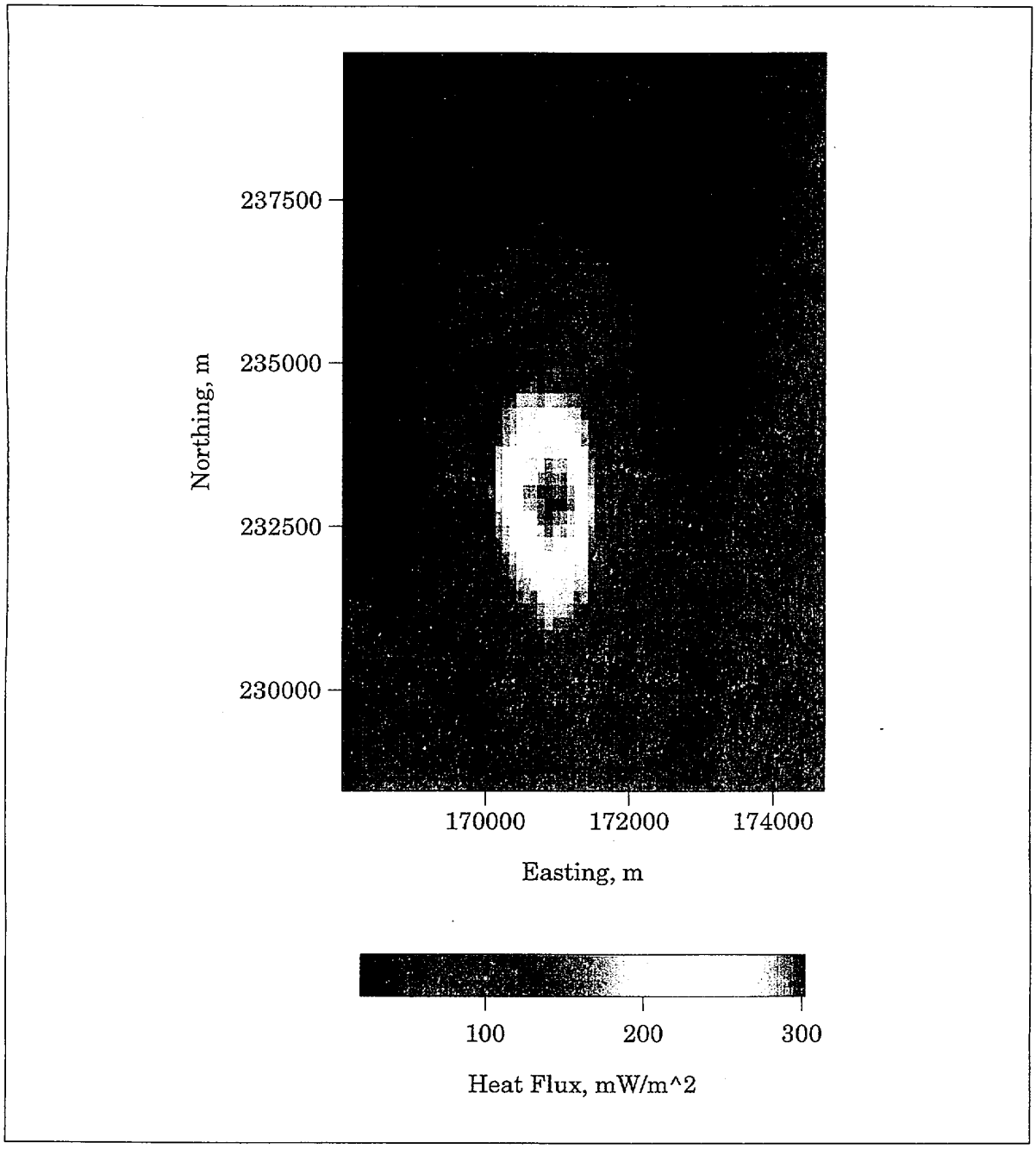

Figure 16. Simulated Heat Flux at Surface After 2000 Years (3-D Conduction Limited).
The figure shows the simulated heat flux at the surface after 2000 yr using the three-dimensional, conduction-limited model. (DTN: LABR150191DN99.001)

of the heat flux if the heat-transfer mechanism is truly one of significant heat-pipe effects. For the analyses of the present study, we chose to use the two-dimensional, thermohydrologic simulations to assess the influence of waste heat on soil temperatures because it tends to bound the maximum possible heat flux and soil temperature at the surface.

Despite the fallback of using the "conservative" heat-transfer model to estimate soil temperatures, the three-dimensional solutions can be used to evaluate the relative effect of heat-load design on surface soil temperatures. To accomplish this goal, we performed a conduction-only simulation in which the same amount of waste is spread over a larger area. Unfortunately, the model does not extend far enough to the West to capture the areas proposed for waste emplacement under the lowest heat-load scenarios (20 Mtu/acre). However, the high heat-load scenario examined so far can be reduced to the SCP design of approximately 60 Mtu/acre by including the so-called "lower block," a proposed region to the east of the Ghost Dance fault. The simulation results are shown in Figure 17. As expected, the heat flux at any location at the surface is reduced when the waste is spread over a larger area. In fact, as a first approximation, the predicted surface heat-flux curve for the high-heat-load case can be scaled by the ratio of the heat loads to obtain the surface heat-flux curve for the low-flux scenario. This fact suggests that predictions for even lower heat-load designs can be assessed simply by reducing the predicted surface flux curve accordingly.

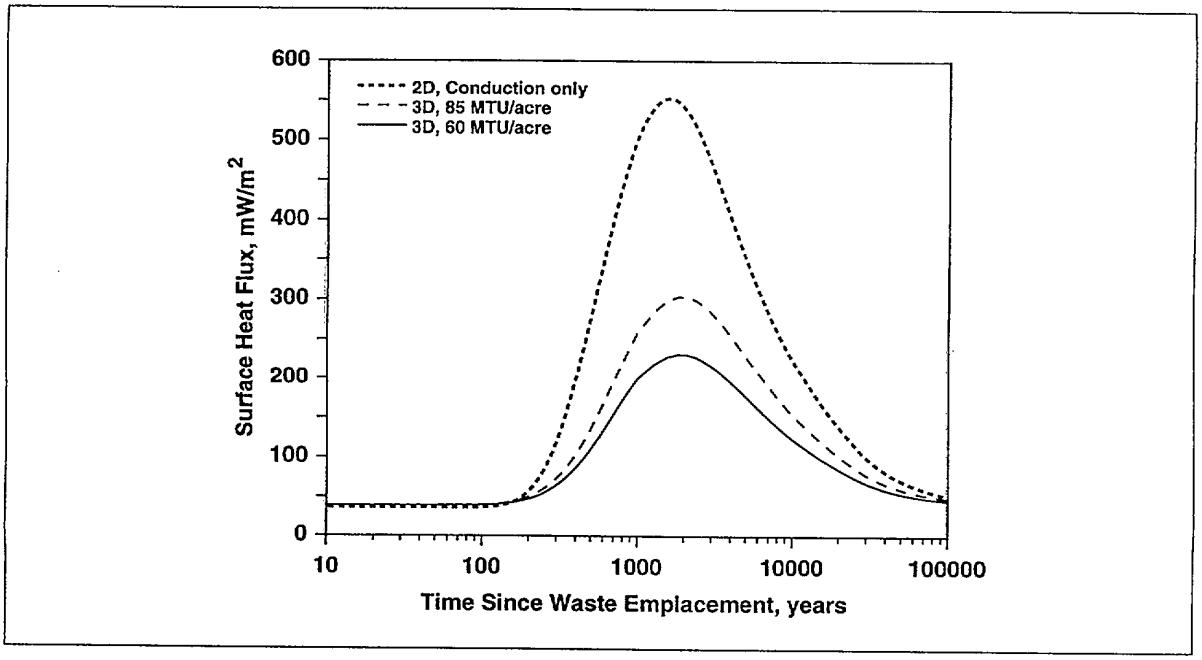

Figure 17. Heat Flux Above Water Table (2-D and 3-D Heat Conduction Only).
The figure shows heat flux versus time directly above the water table for various heat-transfer assumptions: 2-D heat-conduction-only solution and 3-D heat-conduction-only solution for 85 MTU/acre and 60 MTU/acre. (DTN: LABR150191DN99.001)

In summary, the results for the surface heat-flux model relevant to the present study are:

- The heat flux at the surface at any time is greatest directly above the repository and tapers off at the edges and outside the outline of the repository projected to the surface.

- The maximum surface heat flux is about 900 mW/m^2 and occurs about 1000 yr after waste emplacement. Three-dimensional results yield somewhat lower maximum flux values than two-dimensional models due to the spreading of heat in all directions.

- The distance from the repository to the surface appears to have some impact on the results.

- The water-table boundary condition has a minor effect on the model results for the surface heat flux.

- A smeared heat source is adequate for estimating surface heat flux, although in the present study, this simplification is not necessary (results not discussed above).

- Repository designs with lower thermal loads than the base case considered here can be considered approximately by scaling the surface heat-flux curve by the ratio of the thermal loads.

- A full thermohydrologic simulation of heat and mass transport yields higher surface heat fluxes than a conduction-only model due to the preferential upward heat transport caused by the heat-pipe effect.

4. ONE-DIMENSIONAL SOIL-ZONE HEAT-TRANSFER MODEL RESULTS

In this section, we describe the model results for the one-dimensional soil-zone heat-transfer model, including an analysis of the available soil-temperature data. Before predicting specific temperature responses to various heat fluxes and thermal properties, we examine the response of the model to sinusoidal fluctuations in the surface air temperature. We first develop the classical theory and then present an analytical solution that will serve both to highlight the essential features of the soil-temperature model and to provide a verification solution to test the accuracy of the FEHM code.

4.1 MODEL THEORY

Our purpose is to infer the thermal diffusivity of the soil layer in the Yucca mountain region using measurements of temperature as a function of time within the soil layer. To this end, we introduce Kelvin's classical treatment for determining the diffusivity of a half space heated from above (Thomson 1861). The theory assumes that heat transport is purely by conduction, that the surface temperature variation is periodic, and that the periodic temperature variation with depth is in steady state.

Soil temperatures respond at depth to the periodic daytime heating of the sun. Both the lag in the response to the periodic heating of the soil surface and the amplitude of the response at depth can be used to determine the thermal diffusivity of the soil. Independent methods exist for extracting the thermal diffusivity of the layer depending on which parameter, amplitude, or lag one chooses to analyze. Each of these methods has been discussed in detail by Carslaw and Jaeger (1985). Following the derivation of two distinct methods for determining the thermal diffusivity of the soil layer, we review the theoretical and practical implementation of the methods as well as their inherent limitations. Subsequently, we apply each method to the Yucca Mountain soil-temperature data sets and discuss the results.

A typical approximation that allows relevant features of the system to be investigated (e.g., the response to diurnal or seasonal heating) is a periodic temporally varying boundary condition on surface temperature:

$$T_s = T_{avg} + A_0 \sin(\omega t), \tag{5}$$

where T_s is the time-varying surface temperature, T_{avg} is the average surface temperature, A_0 is the amplitude of the variation in the sinusoidal temperature variation, and ω is $2\pi/\tau$, where τ is the period of the oscillation (e.g., 1 day for diurnal changes, 365 days for seasonal changes). The solution to the heat-conduction equation for this boundary condition is (Carslaw and Jeager 1985):

$$T(z,t) = T_{avg} + A_0[\sin(\omega t - z/d_d)]e^{-z/d_d} \quad , \tag{6}$$

where d_d is the damping depth, given by

$$d_d = \sqrt{\frac{\alpha\tau}{\pi}} \quad . \tag{7}$$

Although the actual variability in surface temperature is more complex than can be described with a sinusoidal oscillation, this solution illustrates the key features of the heat-exchange process.

Physically, the damping depth is a measure of the depth into the soil that an oscillation in the surface temperature can penetrate, as evidenced by the exponential term in Eq. 6. It is a function of the thermal diffusivity of the soil and the period of the oscillation so that seasonal variations in soil temperature penetrate into the subsurface to greater depths. Table 2 shows the damping depths for diurnal and seasonal variations in temperature for the different soil-zone thermal-diffusivity values selected in Section 2. The sampling ports in the Yucca Mountain data set are located at depths of 15, 30, and 45 cm. The table illustrates that measurements performed to capture the diurnal changes in surface temperature are adequate for calibrating the thermal diffusivity of the soil. (Note that a depth of Ad_d implies that the strength of the signal will be reduced by a factor of e^{-A}. Thus, for example, at a depth of 45 cm the signal would be reduced to approximately 5% of its surface amplitude for the nominal soil type. This effect is also illustrated in Figure 18, a plot of temperature versus depth for the "wet"-soil thermal diffusivity. A corresponding simulation for a seasonal change in temperature is shown in Figure 19. The thermal pulse imparted by seasonal variations in temperature penetrate to depths of several meters, well below the sampling ports (and into the bedrock at many locations of interest). The 15-, 30-, and 45-cm sampling ports are sensitive to diurnal as well as seasonal temperature variations. However, a coarse sampling rate entails a coarse resolution of the thermal diffusivity of the soil layer because the diffusivity is dependent on the interval of the discrete sampling rate (discussed below). Consequently, only the hourly measurements used to resolve the diurnal signal will be used in the present study.

Table 2. Soil Thermal Diffusivities and Computed Heat-Transfer Parameters.
(DTN: LABR150191DN99.001)

Soil Type	Thermal Diffusivity α (10^{-7} m^2/s)	Diurnal Damping Depth (cm)	Seasonal Damping Depth (cm)	Phase Shift at 45-cm Depth, Diurnal (days)	Phase Shift at 45-cm Depth, Seasonal (days)
Dry	3.5	10	190	0.72	14
Nominal	7.8	15	280	0.48	9
Wet	5.8	13	240	0.55	11

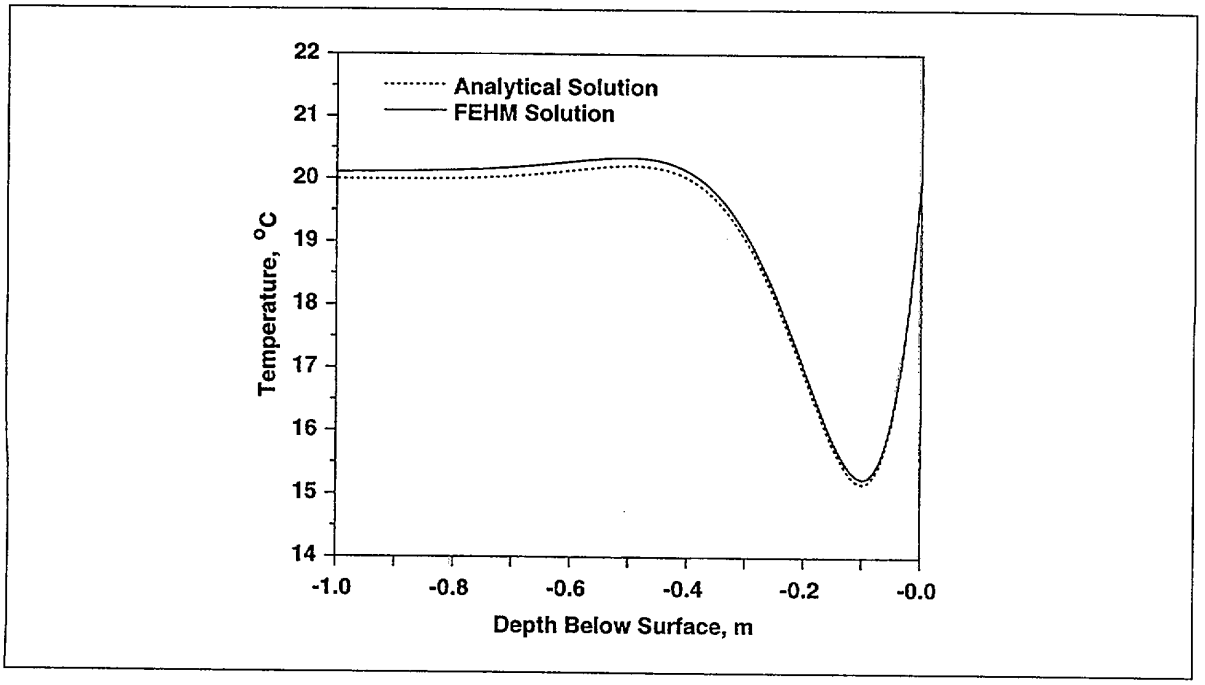

Figure 18. Temperature Below the Surface for a Diurnal Temperature Oscillation. The figure shows temperature versus depth below the surface for a diurnal temperature oscillation imparted at the ground surface. The simulation illustrates that the FEHM numerical model properly captures the heat-transfer behavior at this time and spatial scale. (DTN: LABR150191DN99.001)

In addition to the dampening of the amplitude of the temperature fluctuations with depth is the presence of a phase shift of the temperature response at depth, represented by z/d_d in the argument of the sine function in Eq. 6. The lag of the response, τ_l, is obtained by rearranging Eq. 6 into the following form:

$$T(z,t) = T_{avg} + A_0[\sin\{\omega(t-\tau_l)\}]e^{-z/d_d}, \tag{8}$$

where

$$\tau_l = \frac{z}{\omega d_d} = \frac{z\tau}{2\pi d_d}. \tag{9}$$

Table 2 shows the predicted phase lags at the 45-cm probe for diurnal and seasonal temperature variations, and Figures 20 and 21 show the FEHM and analytical-solution predictions of temperature versus time for the diurnal and seasonal-variation models. The phase lags are clearly evident in the plots and demonstrate that, in principal, measurements of temperature lags can be used to calibrate thermal diffusivity. Actual field data will exhibit temperature variations at a variety of frequencies as well as variations in amplitude due to changing weather, but these effects

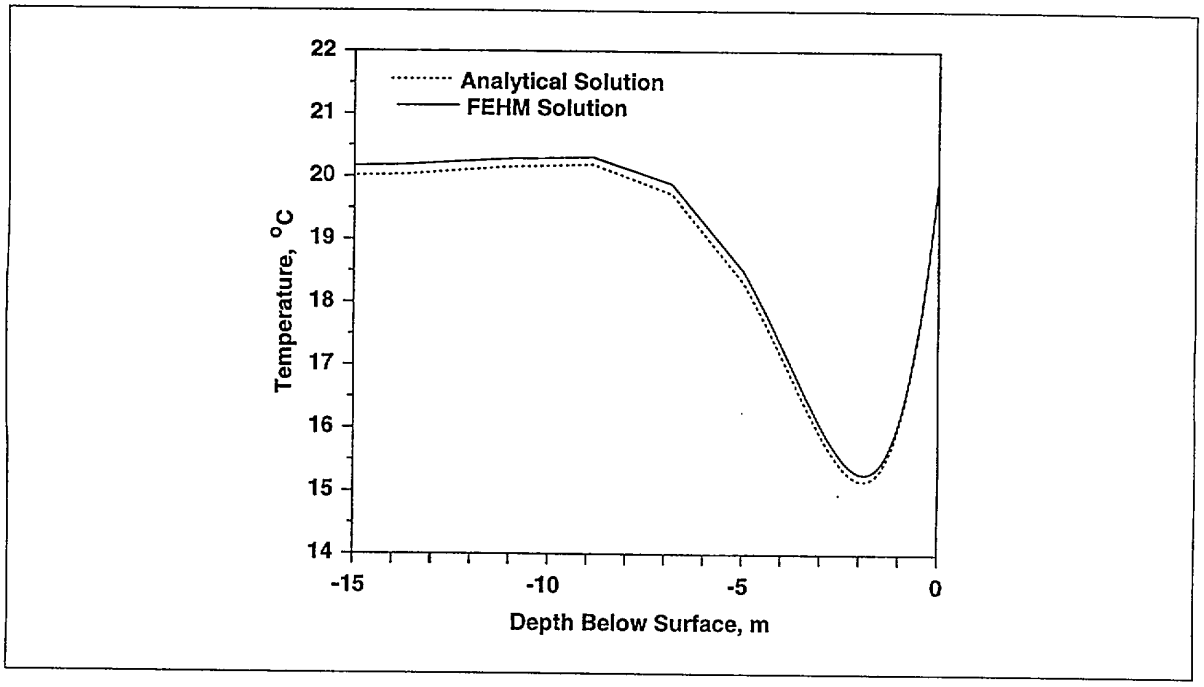

Figure 19. Temperature Below the Surface for a Seasonal Temperature Oscillation. The figure shows temperature versus depth below the surface for a seasonal temperature oscillation imparted at the ground surface. The simulation illustrates that the FEHM numerical model properly captures the heat-transfer behavior at this time and spatial scale. (DTN: LABR150191DN99.001)

pose no particular difficulty in interpretation, as the response can be determined for any harmonic in the frequency domain to obtain α.

Because we are particularly interested in the response to the diurnal signal, we combine Eq. 7 and Eq. 9 to yield

$$\alpha = \frac{z^2 \tau_{24}}{4\pi\tau_l^2}, \quad , \tag{10}$$

where τ_{24} is the assumed 24-hour input signal. Therefore, if the time lag, τ_l, of the temperature signal at depth can be determined relative to the surface temperature, one may calculate the thermal diffusivity of the soil layer.

An alternative derivation of the thermal diffusivity follows by considering the ratio of the amplitudes of identical harmonics of the temperature-time series observed at different depths in the soil layer. Because diurnal surface-temperature variations in the soil layer are approximately sinusoidal, the system is ideal for Fourier analysis. Accordingly, a comparison of the magnitude

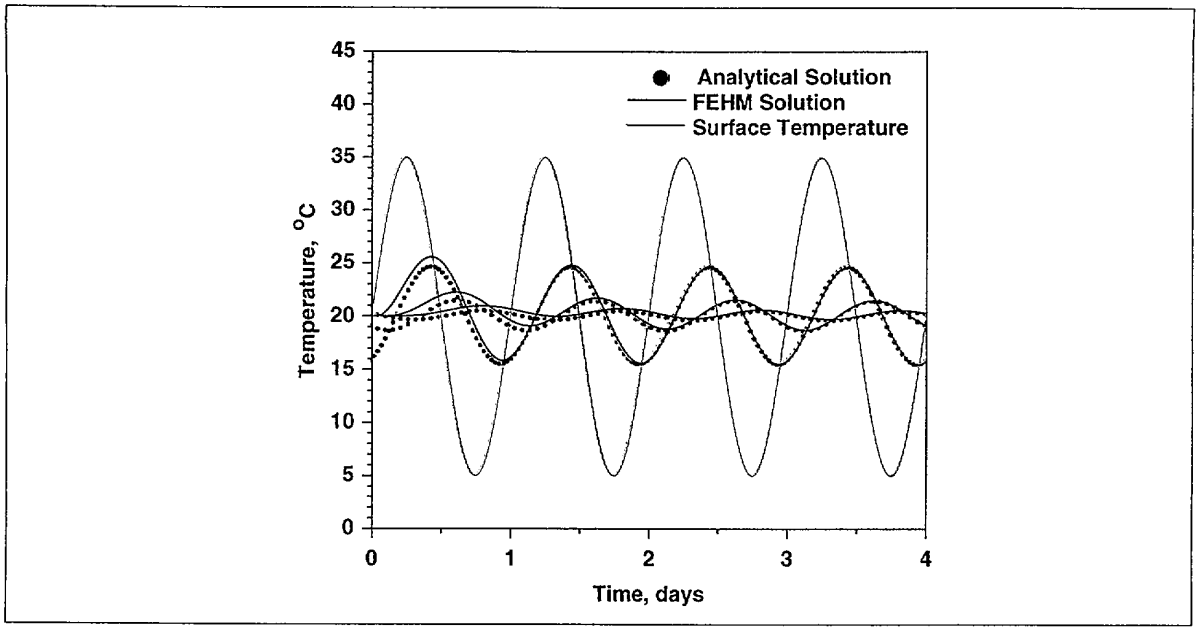

Figure 20. Temperatures for Wet-soil Thermal-diffusivity, Diurnal Temperature Variation. The figure shows temperature versus time at selected depths (15, 30, and 45 cm) for the wet-soil thermal-diffusivity, diurnal temperature variation. (DTN: LABR150191DN99.001)

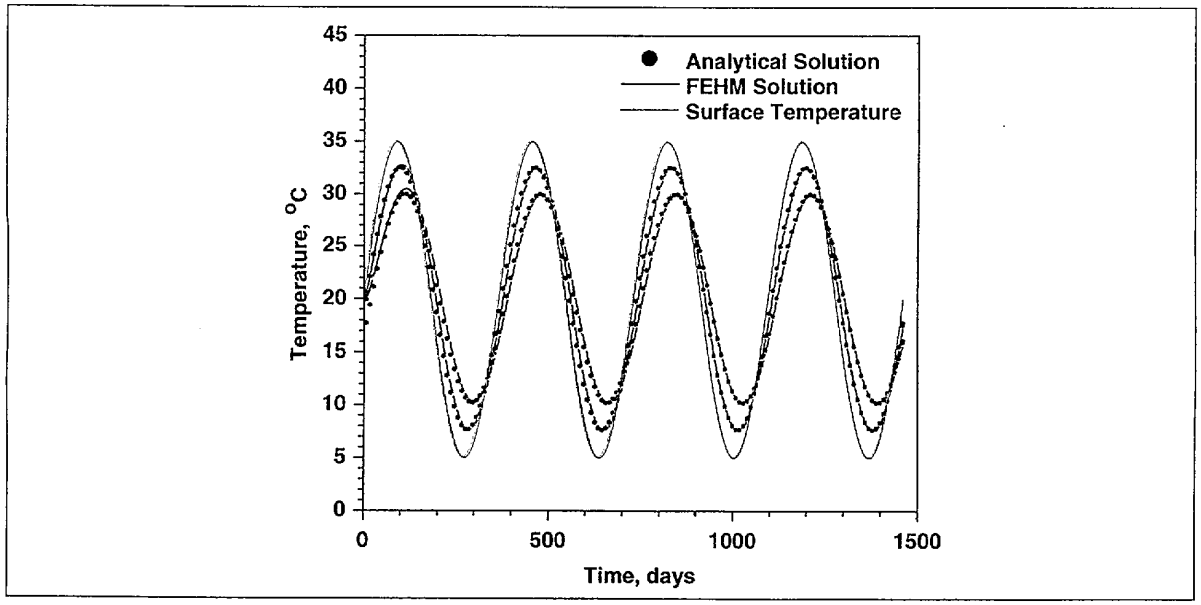

Figure 21. Temperatures for Wet-soil Thermal-diffusivity, Seasonal Temperature Variation. The figure shows temperature versus time at selected depths (45 cm, 1 m) for the wet-soil thermal-diffusivity, seasonal temperature variation. (DTN: LABR150191DN99.001)

of the spectral coefficients of the temperature-time series can be used to determine the soil diffusivity. A means of determining the thermal diffusivity of the soil layer based on the amplitude of the diurnal perturbation of the soil surface temperature follows.

From Eq. 6, we may write the temperatures T_1 and T_2 at depths z_1 and z_2 in the forms:

$$T_1 = T'_{avg} + T' \sin(\omega t - z_1/d_d) \qquad T_2 = T''_{avg} + T'' \sin(\omega t - z_2/d_d). \tag{11}$$

Comparing coefficients from Eq. 6 and Eq. 11 gives

$$T'_{avg} = T''_{avg} = T_{avg} \qquad T' = A_o e^{-z_1/d_d} \qquad T'' = A_o e^{-z_2/d_d}. \tag{12}$$

The latter pair of expressions in Eq. 12 can be combined to yield

$$\frac{z_2 - z_1}{\ln T' - \ln T''} = d_d = \sqrt{\frac{\alpha\tau}{\pi}} \quad . \tag{13}$$

If we then let $z_1 = 0.0$ in Eq. 13 (so that T' is calculated at the surface of the soil and equals the amplitude of the temperature harmonic with a diurnal period), we obtain the following expression for the thermal diffusivity:

$$\alpha = \left[\frac{z_2}{\ln(T'/T'')}\right]^2 \frac{\pi}{\tau_{24}} \quad . \tag{14}$$

In practice, the coefficients T' and T'', corresponding to the harmonic with a 24-hour period, are obtained from a fast Fourier transform (FFT) of the time series of the temperatures. Equations 10 and 14 constitute distinct expressions for the diffusivity of the soil layer analyzed. In the following section, we discuss practical constraints on employing each of the theoretical methods required to obtain values for either τ_l or T' and T''.

4.2 PRACTICAL MODEL CONSTRAINTS

The time lag of the temperature at depth relative to the surface temperature has been determined below by calculating the cross covariance of the air temperature and 45-cm-depth soil-temperature time series. The temperature-time series provided in the Yucca Mountain data set were recorded hourly; therefore, the discrete cross covariance calculated can only yield lag times corresponding to integer multiples of an hour. Consequently, only a discrete set of thermal diffusivities may be recovered from the lag response of the soil temperatures at depth (because the values of τ_l become discrete in Eq. 10).

To obtain a thermal-diffusivity value representative of soils in the region, the squared time lags determined at the 10 sites are averaged. However, it should be noted that although the averaging results in a diffusivity corresponding to a noninteger value for the time lag, it is not an improvement on the accuracy of the discretized time lags. That is, the average thermal diffusivity calculated has limited accuracy because the terms being averaged are affected by the discretization. Furthermore, the average diffusivity cannot be calculated as the diffusivity inferred from the average lag. Instead, we calculate a true average of individually calculated diffusivities. This point must be considered because τ_l is squared in Eq. 10, and the square of the average is not equal to the average of the squares.

In theory, determining the amplitude of the response at depth relative to fluctuations at the surface does not introduce the errors inherent in determining the lag response of the temperature with depth. For example, the amplitudes of the harmonic associated with diurnal fluctuations in the temperature field can be calculated independently at different depths and then substituted into Eq. 14 to determine thermal diffusivity. Therefore, any errors associated with the calculations must result from either a lack of resolution of the diurnal signal, errors due to data recording, or errors due to data interpretation. Because twenty-four data points easily resolve the diurnal temperature fluctuation, we need only consider the interpretation of the data as a possible source of error (comments on data accuracy are beyond the scope of this report). After calculating thermal diffusivity values in the following section, we return to considering the errors associated with data interpretation as they pertain to the calculations described above.

4.3 INVERSION OF TEMPERATURE-TIME SERIES DATA FOR SOIL THERMAL DIFFUSIVITY

For this analysis, we use the air-temperature data collected at two surface sites and ten temperature probes at 0.45-m depth. The summer temperature-time-series data consist of 14 days sampled at one-hour intervals. Figure 22, a plot of the temperature-time series, makes it clear that the dominant period is the 24-hour diurnal temperature variation.

The time lag of the temperature at depth relative to the surface temperature is determined by calculating the cross covariance of the air-temperature and soil-temperature time series. The discrete cross covariance is defined by

$$c_{xy}(m) = \begin{cases} \sum_{n=0}^{N-|m|-1} \left(x(n) - \frac{1}{N} \sum_{i=0}^{N-1} x_i \right) \left(y_{n+m}{}^*(n) - \frac{1}{N} \sum_{i=0}^{N-1} y_i{}^* \right) & m \geq 0 \\ c^*{}_{xy}(-m) & m < 0 \end{cases} \quad . \quad (15)$$

By finding the time lag at which the two functions, surface temperature and temperature at depth, are most correlated, an estimate of the time lag is made, from which the soil thermal diffusivity is obtained using Eq. 10.

The data set consists of two time series of air temperature and ten time series of soil temperature measured at a depth of 0.45 m. All measurements cover the same time period from August 26, 1997, at 1:00 A.M. through September 8, 1997, at 8:00 A.M. Temperatures were recorded every hour, resulting in a total of 319 measurements at each temperature probe. Figure 22 shows the entire data set. The air temperature has much higher amplitude fluctuations (±15°C) and is cooler on average. The soil-temperature measurements have daily fluctuations that are much smaller (±2°C). It is apparent that the temperature fluctuation is dominated by the 24-hour diurnal variation. The data appear to also show a longer-term variation with temperatures, generally decreasing from day one to day nine and then increasing again from day nine to fourteen.

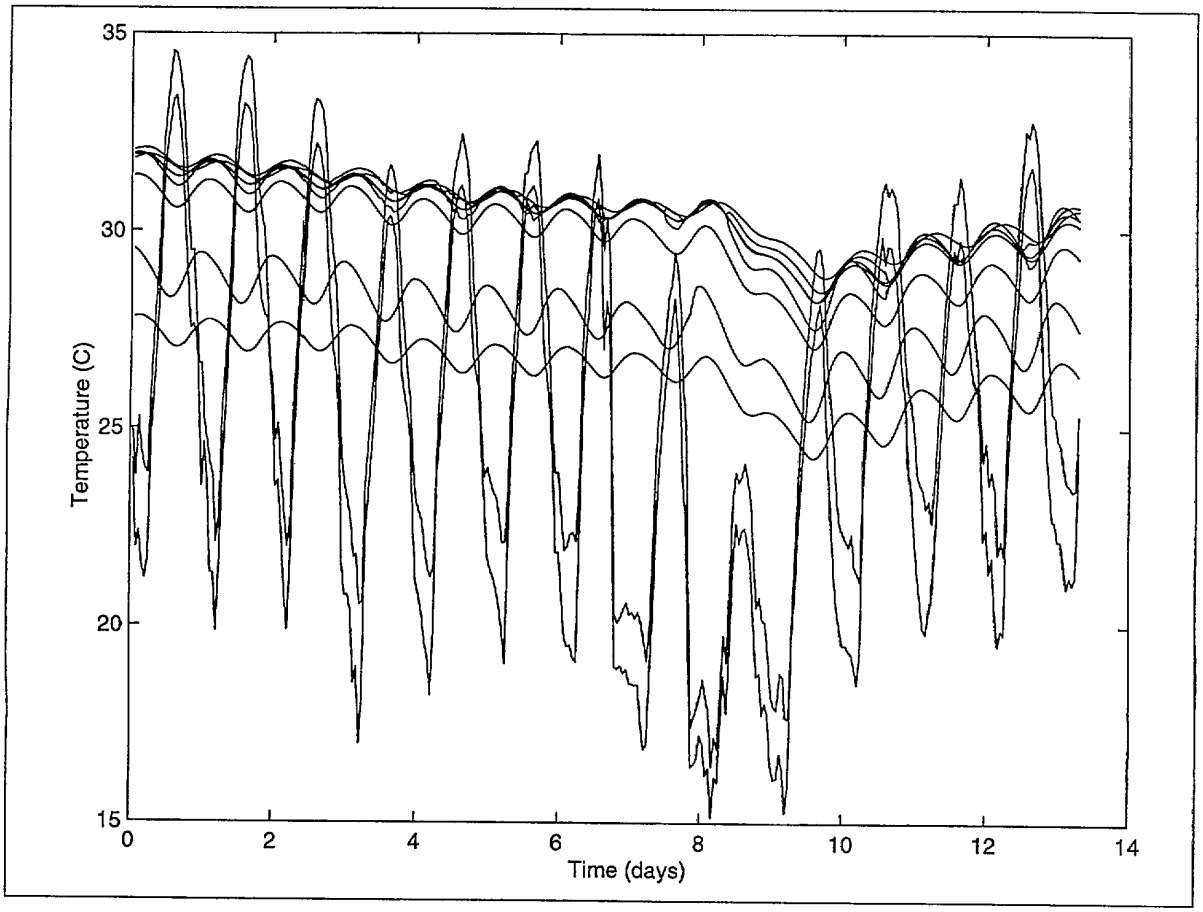

Figure 22. Air and Soil Temperature Measured Over a 14-day Period.
The figure plots air temperature (high-amplitude variation) and soil temperature (low-amplitude variation) measured over a 14-day period. Temperature variation is dominated by diurnal variations. (DTN: MO9812PSNTGH45.000)

The cross covariance of air temperature to soil temperature for a single soil measurement is shown in Figure 23. The cross covariance is also dominated by the diurnal, twenty-four-hour period. The maximum correlation occurs at a time lag of thirteen hours. Figure 24 shows the

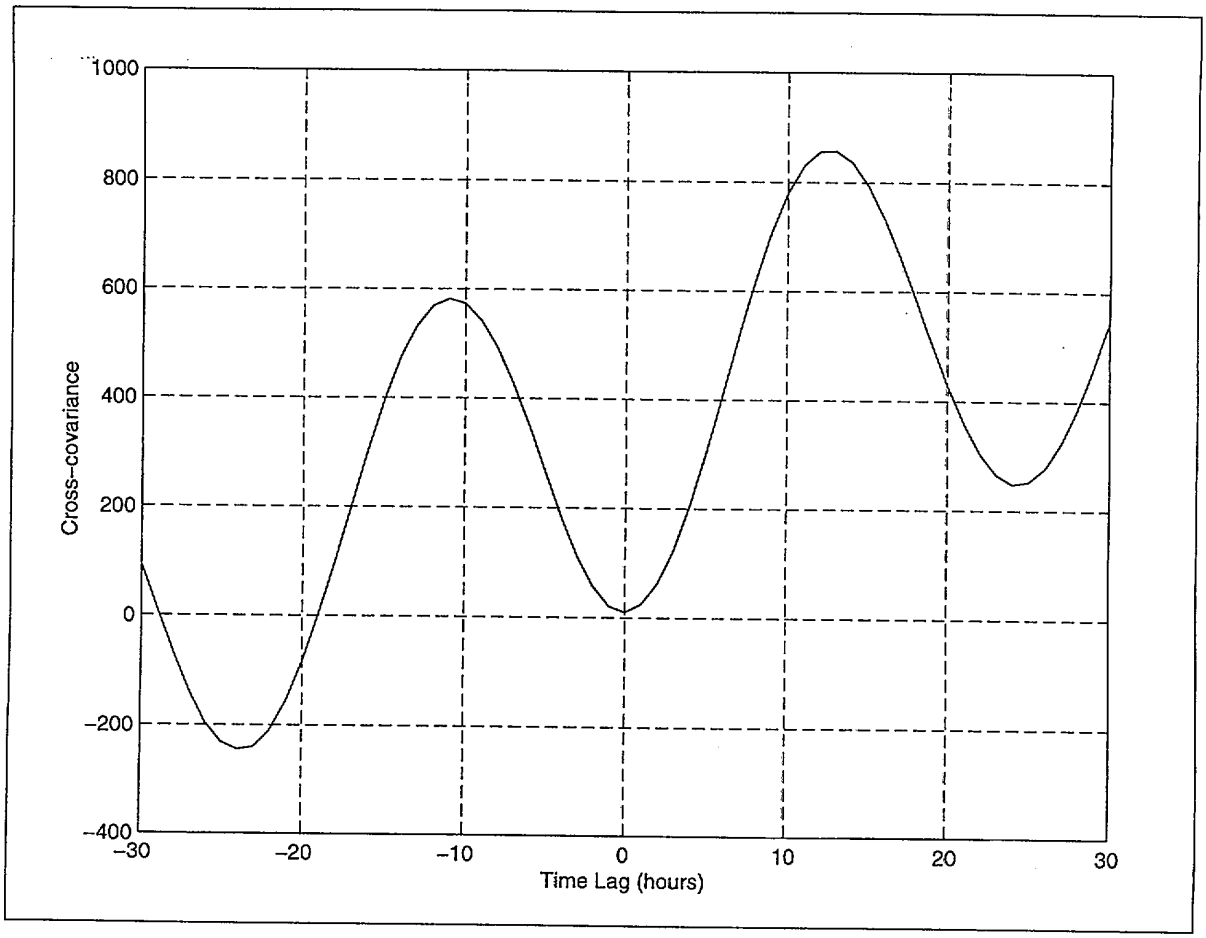

Figure 23. Cross Covariance of Air Temperature to Soil Temperature.
The figure plots the cross covariance of air temperature to soil temperature. Note that the signals are most correlated at a time lag of 13 hr. (DTN: LABR150191DN99.001)

cross covariance of six of the soil-temperature measurements. There is some variation in the time lag at which the time series are most correlated.

The next step of the analysis is to calculate the time lag at which each soil-temperature time series is most correlated with each air-temperature time series (Figure 25). With ten soil-temperature measurements and two air-temperature measurements, twenty time lags are calculated. The maximum correlation occurs at the same time regardless of which air-temperature time series is used. The average lag for all twenty is 13.8 hr with a standard deviation of 1.48 hr. The average thermal diffusivity based on Eq. 10 is $5.81\times10^{-7} m^2 s^{-1}$, with a standard deviation of $1.19\times10^{-7} m^2 s^{-1}$, where it has been assumed that $z = 0.45$ m and $\tau_{24} = 24$ hr.

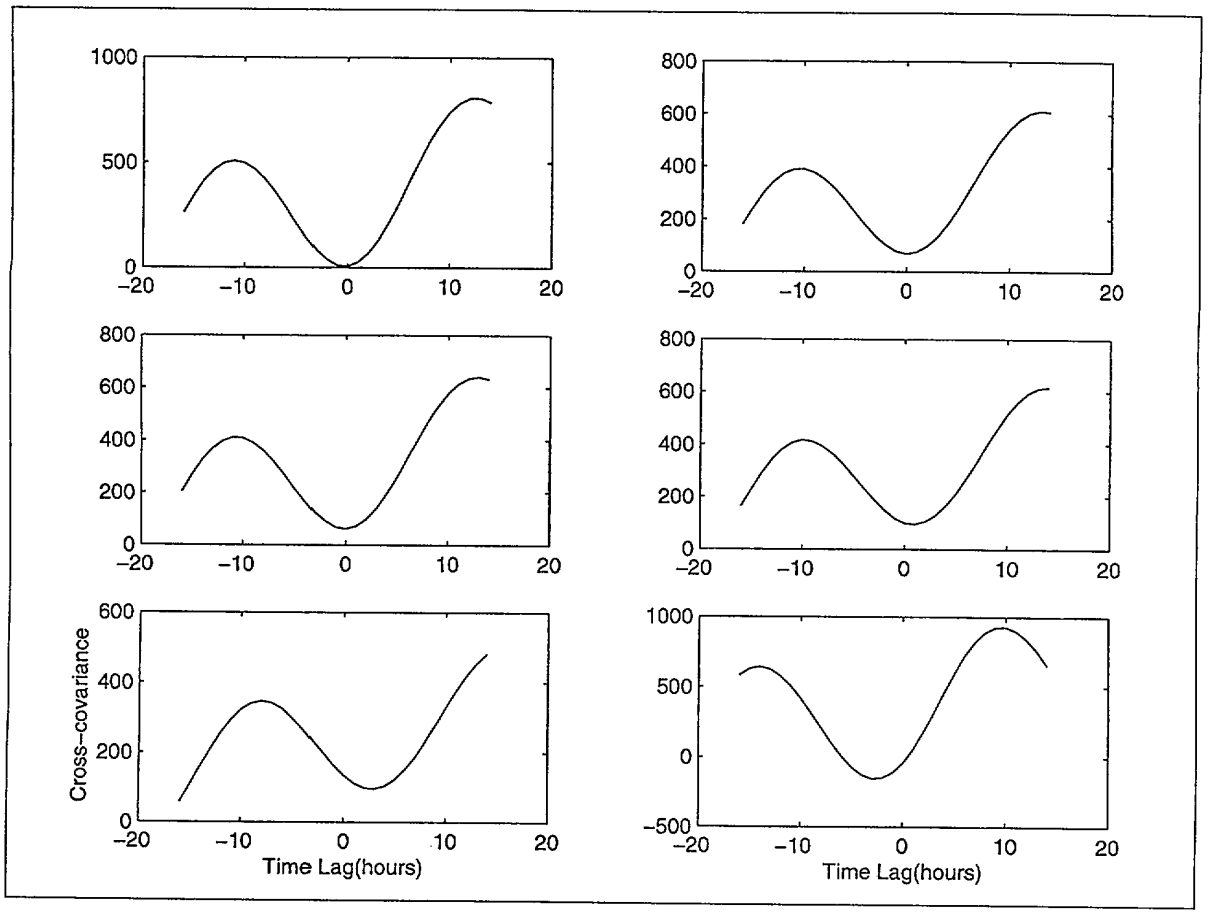

Figure 24. Cross Covariance of Air Temperature to Six Soil-temperature Time Series. The figure shows the cross covariance of air temperature to six soil-temperature time series. The maximum correlation of the signals varies between 10 and 16 hr. (DTN: LABR150191DN99.001)

These results, obtained from analyzing the lag in the temperature response at depth, have been re-examined using the amplitude of the thermal response at depth to determine soil diffusivity (Eq. 14).

From determining the amplitude of the variations in the temperature-time series at the 10 sites represented in the Yucca Mountain data set (Appendix, Table 1, DTN MO9812PSNTGH45.000), we find an average thermal diffusivity of $9.98\times10^{-7} m^2 s^{-1}$ with a standard deviation of $1.68\times10^{-7} m^2 s^{-1}$. Clearly, the sensitivity of this method to data interpretation gives flawed results. The assumption that the magnitude of the air-temperature fluctuations can be used as a substitute for the magnitude of surface soil-temperature variations is the likely source of error. For example, differences in radiative absorption between air and soil are not considered. Because solar radiative heating typically raises the temperature of the ground more quickly than the air, using air temperatures in place of surface soil temperatures will underestimate the surface soil temperature. Consequently, fluctuations in the soil-temperature data at depth appear relatively

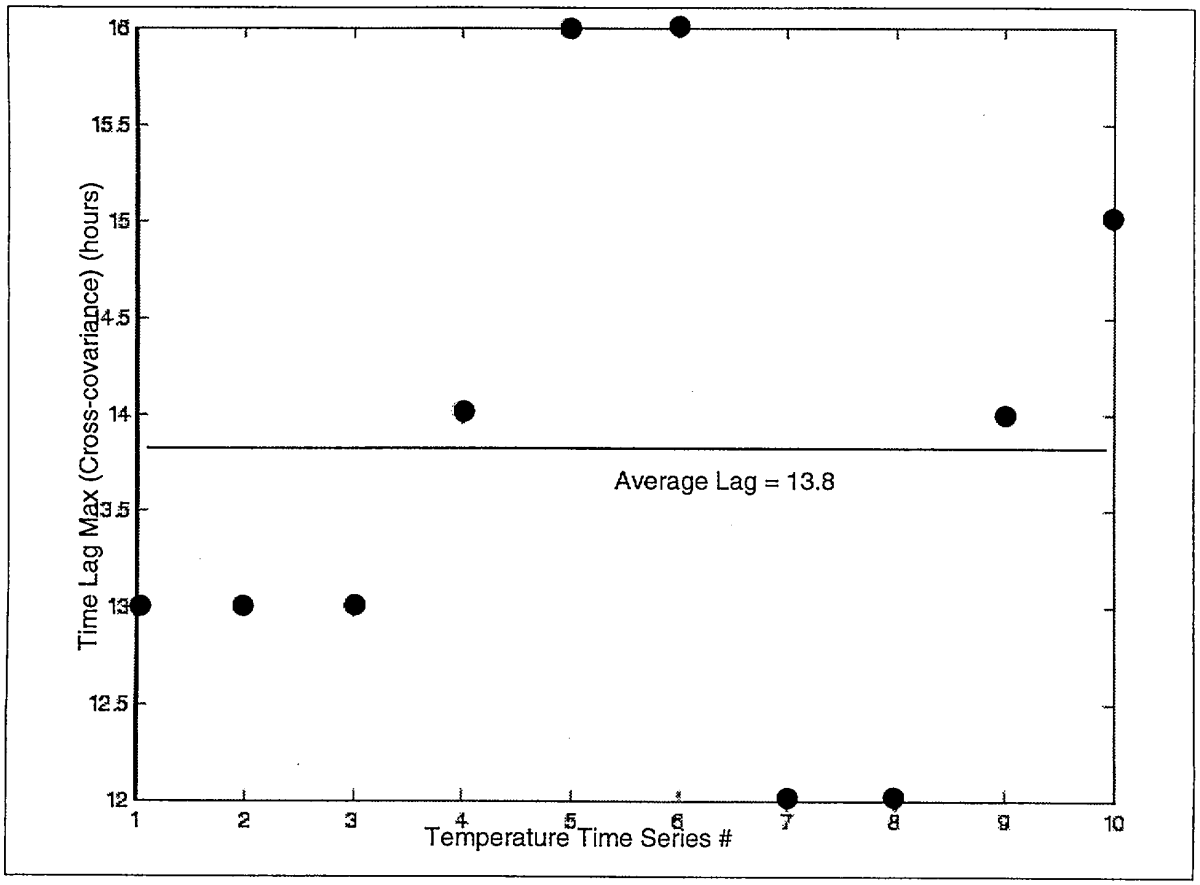

Figure 25. Time Lag of Maximum Correlation.
The figure plots the time lag of maximum cross correlation for each of the nine temperature-time series. (DTN: LABR150191DN99.001)

large compared with (the air-temperature) fluctuations at the surface, implying a higher thermal diffusivity than is actually the case.

The Appendix of this report includes the analysis of three data sets containing air and soil temperatures recorded during one-week periods in December 1997, January 1998, and February 1998 (Appendix, Tables 2–4). These additional data were intended to further constrain the thermal-diffusivity value for the soil layer in the Yucca Mountain region. However, the three data sets from the Winter 1997-to-1998 period have not been considered in arriving at the estimated thermal-diffusivity value quoted above. This decision was based on observations of inconsistency in the winter data sets. For example, we find that the December data set contains numerous flawed data values exhibited by artificial spikes in the temperature-time series. In contrast, the time series for the January data set are smooth but exhibit no diurnal variations, perhaps due to snow cover at the data-gathering sites. Finally, the February data appear smooth

and show diurnal variations; however, the inferred thermal diffusivity is exceptionally large, a possible result of winter-weather-related data gathering.

4.4 SUMMARY AND DISCUSSION OF SOURCES OF ERROR

The goal of the data analysis described herein is to determine a representative soil-layer diffusivity for the Yucca Mountain region. Because the soil in the Yucca Mountain region is expected to vary locally to some degree, both laterally and in depth, the soil-layer diffusivity determined must be considered a representative or idealized value. Attempting to determine a single representative value for this parameter from a data set influenced by the heterogeneity of the Yucca Mountain soil requires certain assumptions during the data analysis. For example, the study focuses on the diffusivity of the soil layer from the surface down, rather than examining the diffusivity of strata within the soil layer. An analysis of the latter variety would not be subject to the errors described above that are inherent with the assumption that the surface air temperature can be used to represent the surface soil temperature; however, it would be affected by variations in the composition of the local soil layer with depth. For example, by considering the total soil layer for a depth extending to 45 cm, it is assumed that a soil diffusivity will be extracted from the data that represents the integrated properties of the combined layers of sand, humus, and clay comprising the soil layer affected by diurnal temperature fluctuations. Because a dry sandy surface layer would have a particularly low thermal diffusivity, it is important that this layer be included in the thermal-diffusivity calculation by considering the response at depth compared to the soil surface.

Given the findings and discussion presented in the previous sections, it is apparent that comparing the amplitude of the temperature variations at depth to the amplitude of the surface air-temperature variation will lead to an overestimate of the thermal diffusivity of the soil layer. However, it is likely that soil-surface-temperature variations will be in phase with air-temperature variations because the surface air temperature may be assumed to be tightly coupled to the soil temperature. Furthermore, local air-temperature variations were found to be in phase at different locations despite displaying differing amplitudes. Thus, the assumption that the lag of the temperature response at depth can be compared to the air-temperature fluctuations in place of surface-soil-temperature variations appears well founded.

We conclude that the phase shift of the diurnal temperature cycle at depth can be used to estimate the thermal diffusivity of the Yucca Mountain soil layer. However, the accuracy of the thermal diffusivity derived from the temperature data set is subject to a number of factors. The cross-correlation technique limits possible lag times to a discretized set of values with a resolution equal to the sampling time of the recorded thermal signals. As a result, only a coarse set of thermal diffusivities is obtainable from the data provided. An increase in sampling rate would increase the accuracy of the soil-layer thermal diffusivity determined from the data. However, the increase in accuracy in the lag times recorded at each of the data sites may not necessarily yield a more accurate representative soil diffusivity for the region (given the implicit error associated with representing the varying diffusivity of the region with a single value).

The large range of lag times calculated in the Appendix indicates the variability in the soil composition at the sites examined. The lag times calculated in this report vary by as much as 16% from the average lag time of the 10 data sets. It is possible that an increase in the sampling rate at each of the data sites may reduce the calculated range of lag times. However, the apparent range of values is most likely a manifestation of the variety in soil composition and exposure at each of the studied sites. The former factor is not a source of error, but the latter factor could be a significant source of error if the soil surface is blocked from exposure to radiative heating for only part of the day (e.g., morning hours). In such a case, heating of the soil surface could be out of phase with heating of the ambient air. For example, a west-facing slope may be warmest in the late afternoon rather than at midday. These considerations require radiative exposure to be controlled at each site to obtain accurate values for the soil diffusivity. The greatest source of error in these calculations results from approximating the temperature of the soil surface by the air temperature—specifically, because the ground absorbs a greater amount of radiative heating than the air. To improve the accuracy of the soil-diffusivity calculations discussed herein, we recommend the removal of the influence of radiative heating at each data-gathering site. This recommendation could be accomplished by providing a large shade that covers each data-gathering site. The shaded area should extend at least a few meters out from the data-gathering site in all directions. (This recommendation assumes that lateral diurnal heating from radiative soil absorption would not extend further than 10 damping depths.)

We conclude that the thermal diffusivity value of $5.81\times10^{-7} m^2 s^{-1}$, based on the lag times from the summer data sets, is the best approximation we can obtain for a representative thermal diffusivity of the Yucca Mountain region soil layer given the present data set. Local differences in diffusivity vary by at least 16% from the quoted value. Furthermore, the data sets analyzed here indicate that there could be significant seasonal variation in the thermal diffusivity of the soil layer, depending on the moisture content of the soil and the presence of frost or snow cover. For future analyses, we recommend removing the influence of radiative heating of the ground at data-gathering sites. This approach would allow for more accurate calculations and would also allow for the use of both of the theoretical methods described above.

4.5 MODEL RESULTS

Because some of these analyses were performed before the measured data were available, we continue to use the dry, nominal, and wet thermal-property values of Table 1. In addition, we note that the available field data analyzed in the previous section support the use of the wet-soil property values, in that the measured thermal-diffusivity value (from the time-lag analysis method) is extremely close to the estimated diffusivity using typical "wet-soil" properties. Therefore, the data suggest that the wet-soil curve is most likely, but we retain the dry and nominal property values in the presentation below to bound possible variability with soil moisture conditions.

We begin this analysis with simulations of the average soil-zone temperature profile using a heat-flux boundary condition at the bottom of the model domain. We assume either ambient conditions (35 mW/m^2) or the maximum predicted heat flux at the surface (about 900 mW/m^2). Figure 26 illustrates the impact of the thermal diffusivity on the predicted results.

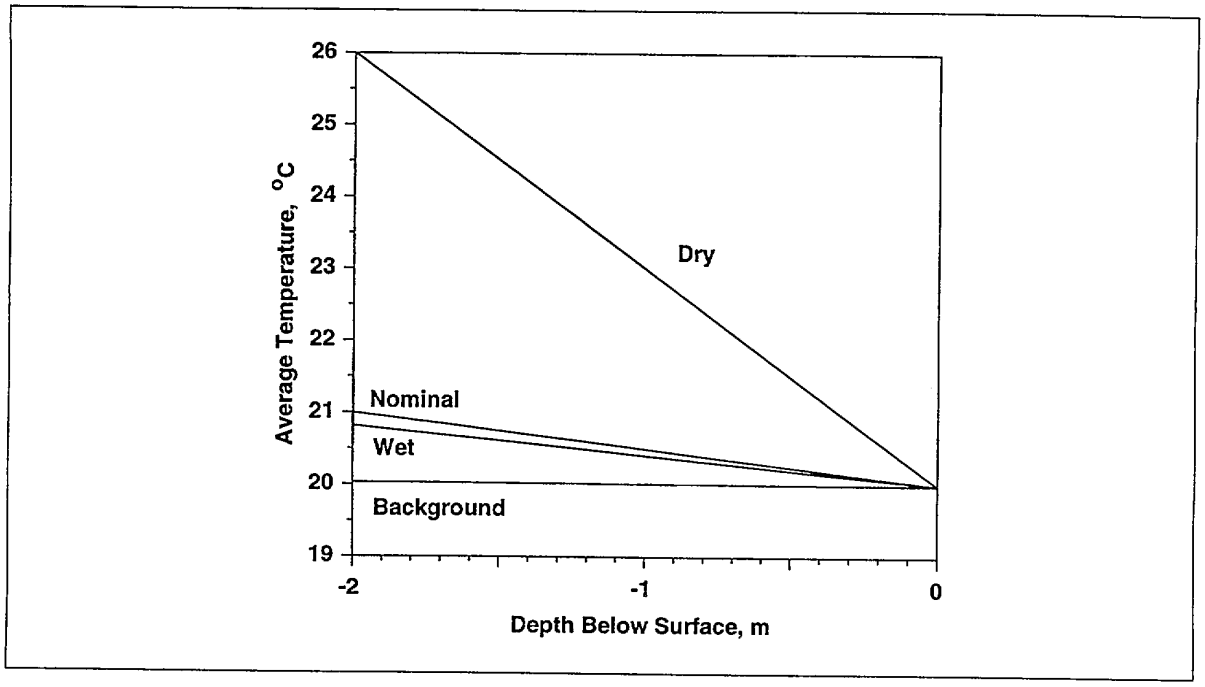

Figure 26. Steady-state Soil-zone Temperature Profiles for Different Soil Wetness.
The figure shows predicted steady-state soil-zone temperature profiles for different soil wetness (different thermal conductivities): background case—35 mW/m^2, repository case—900 mW/m^2.
(DTN: LABR150191DN99.001)

Fixing the surface temperature at the air-soil interface effectively constrains the extent of the temperature rise. In fact, for the simplifications of constant heat flux and surface temperature, the thermal gradient within the soil is easily predicted by integrating Eq. 2 to yield:

$$T = T_s + \frac{q_s}{k} z, \tag{16}$$

where q_s is the heat flux at the surface due to either the ambient geothermal gradient or the repository heat. Taking 1 m as a depth of interest for assessing soil-zone temperature rise, the predicted maximum rise in soil temperature from this analysis is 0.4°C for the wet soil (and also the field-measured soil) and 3°C for the dry soil. The result is also linearly dependent on depth, so that at 0.5-m depth, the rise goes from 0.2°C to 1.5°C, and at 2-m depth, the range is from 0.8°C to 6°C. To tighten these bounds further, field-scale measurements of the thermal diffusivity are required under different soil moisture conditions. We expected the thermal conductivity of the dry soil to provide an upper bound on the soil-temperature rise, and in fact, the field estimates support this assumption. A systematic field-temperature measurement program augmented by tighter estimates of the moisture content from existing studies such as those of Flint et al. (1996) would reduce this uncertainty.

Of course, the temperature in the soil varies due to diurnal and seasonal temperature variations and will be influenced strongly by storm events, which will be accompanied by lower surface temperatures and, perhaps more importantly, by transient changes in the thermal properties of the soil due to the strong dependence of moisture content on thermal properties. This response was illustrated using the analytical solution above. We now compute the time-dependent seasonal changes in temperature at various depths at the maximum repository heat load of 900 mW/m^2. Results of these simulations are shown for depths of 45 cm, 1 m, and 3 m in Figure 27 (dry soil), Figure 28 (nominal soil), and Figure 29 (wet soil). For comparison in Figure 27, we also show the oscillatory behavior predicted for ambient conditions.

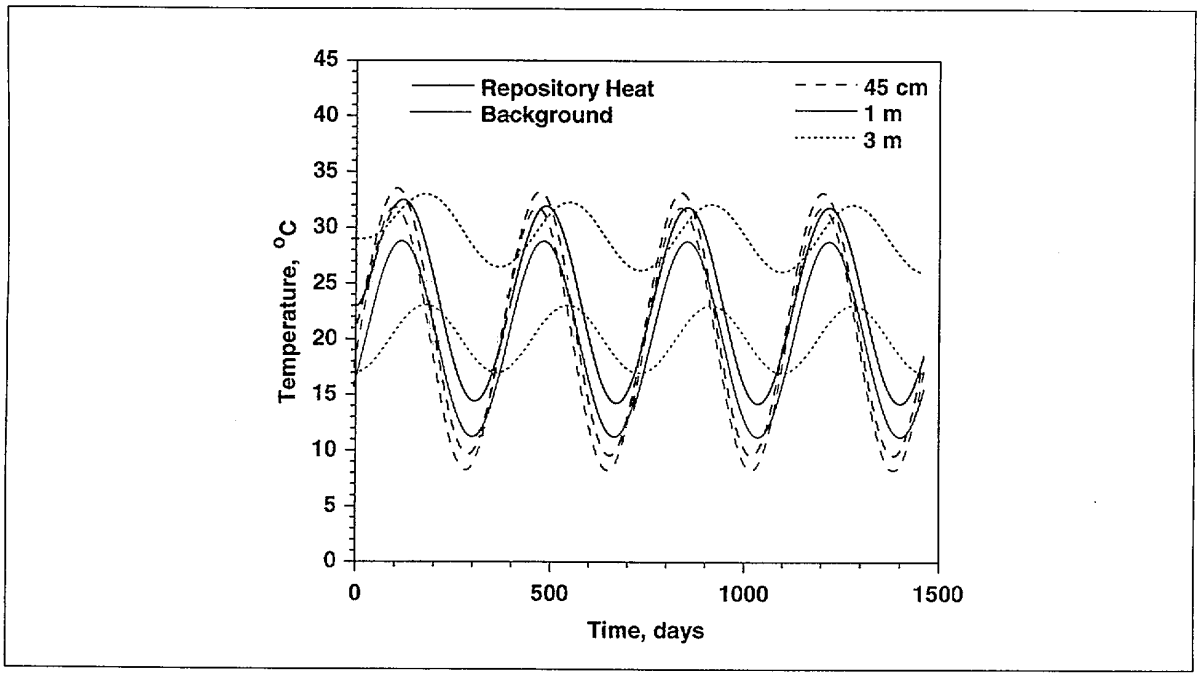

Figure 27. Soil Temperatures for Dry Soil and Maximum Repository Heat Load.
The figure gives predicted soil temperatures in response to seasonal temperature variations at 45-cm, 1-m, and 3-m depths at the maximum repository heat load using dry-soil thermal properties. Red curves are predicted temperatures in the absence of repository heat.
(DTN: LABR150191DN99.001)

The character of the temperature response with depth is very similar to the ambient case, with the additional complication of an increase with depth of the average temperature at any point due to the repository heat. However, to a close approximation, the thermal response at any depth in the presence of repository heat is simply governed by the damping depth analysis presented above about a mean temperature given by the steady-state prediction of temperature rise. In other words, oscillations damp with depth and exhibit lag, and the average temperature increases linearly with depth. This result is expected based on the principle of superposition in a linear system.

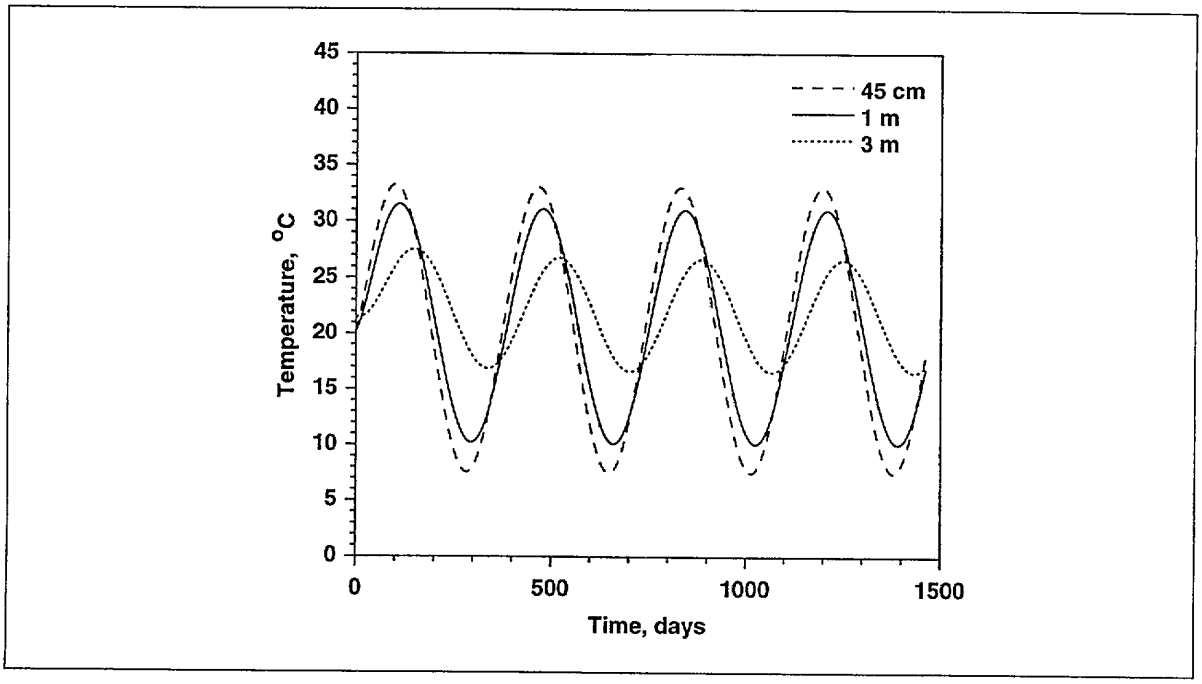

Figure 28. Soil Temperatures for Nominal Soil and Maximum Repository Heat Load. The figure shows predicted soil temperatures in response to seasonal temperature variations at 45-cm, 1-m, and 3-m depths at the maximum repository heat load using nominal-soil thermal properties. (DTN: LABR150191DN99.001)

One final sensitivity calculation examined the nature of the coupling of the atmospheric temperature to the soil-surface temperature. The simulations presented so far assumed high heat-transfer coefficients so that the surface temperature equalled the air temperature. An additional simulation was performed in which the minimum heat-transfer coefficient, assumed to be due to natural convection of air from a heated surface, is applied instead. For the maximum repository heat load, the low heat-transfer coefficient was still large enough to provide efficient heat transfer so that the soil-surface temperature was only 0.3°C greater than the air temperature. Because the heat-transfer coefficient is likely a minimum bound, the soil-surface temperature may be assumed to be tightly coupled to the atmospheric temperature. This result must be viewed in light of the analysis of the difficulties in interpretation of some of the field data, however. Temporary snow cover, or regions with significant radiative heating effects, must ultimately be considered when assessing the thermal effects of heat at a particular time and location.

Finally, we note that the temperature rise at the maximum heat load was presented above, but in reality, this temperature rise will vary with time due to the time-varying heat load from the repository and changes in the moisture content of the soil. Because the time scale of changes in repository heat flux emitted to the surface are large compared to the thermal response time and because the temperature rise varies linearly with surface heat flux (Eq. 16), the time-varying surface heat flux can be scaled to obtain the average temperature rise at any depth. This approach is demonstrated in Figure 30 for the wet-soil properties at 2-m depth at the position directly above

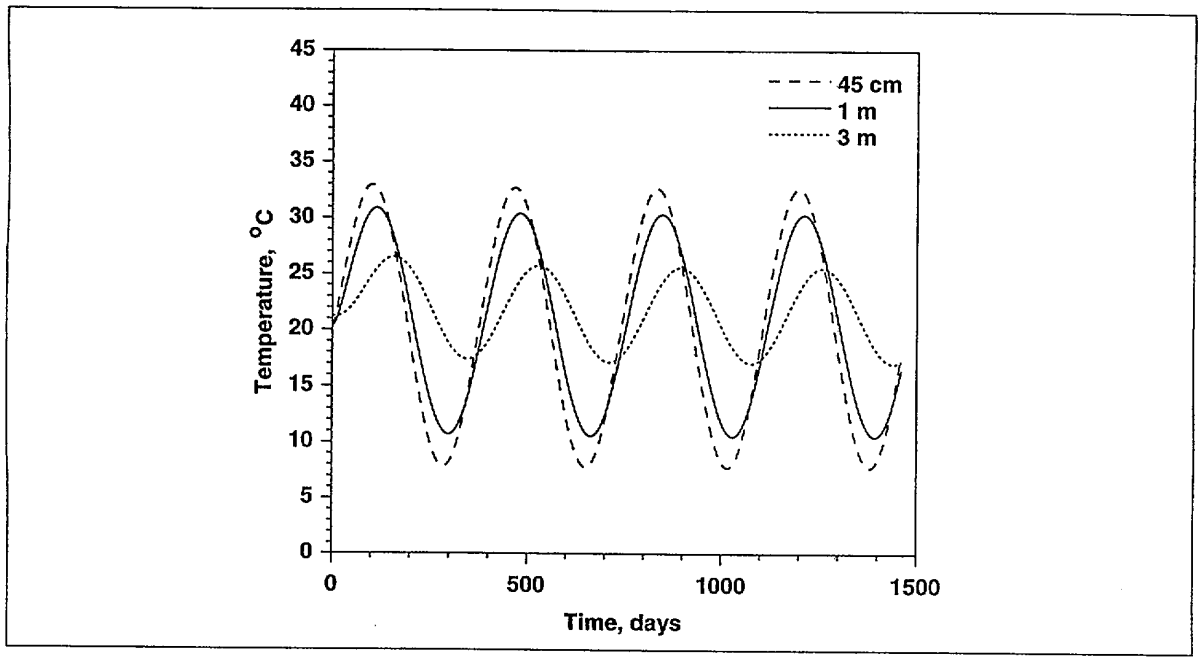

Figure 29. Soil Temperatures for Wet Soil and Maximum Repository Heat Load.
The figure shows predicted soil temperatures in response to seasonal temperature variations at 45-cm, 1-m, and 3-m depths at the maximum repository heat load using wet-soil thermal properties. (DTN: LABR150191DN99.001)

the potential repository. As discussed above, variations about this average temperature are then estimated using the damping-factor analysis. This method can be used to estimate the thermal response at any location above the repository after making an estimate of the time-varying heat flux at that position. No rise is predicted until after several hundred years. Then, a predicted rise in temperature of 0.8°C occurs within about 1000 yr. This rise is followed by a gradual decline in the effect from 1000 to 10,000 yr after waste emplacement. We reiterate that these temperature rises are for the wet-soil properties, which yielded thermal properties close to those estimated from the field data. During extended dry periods, thermal conductivity could be considerably lower, and the corresponding temperature rise would be greater.

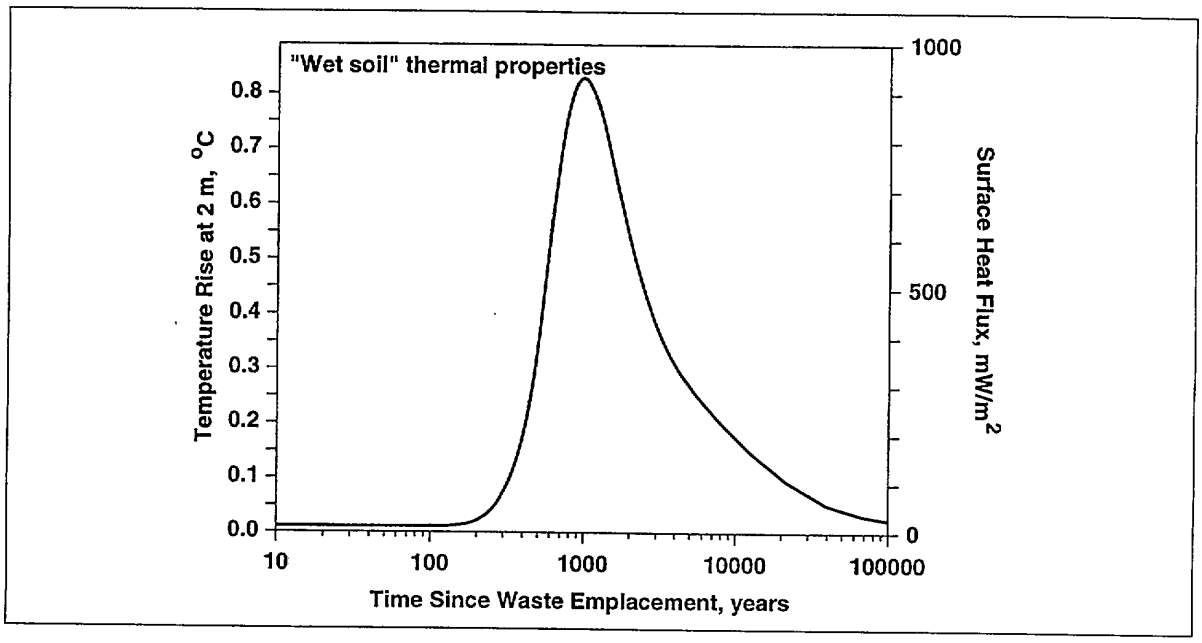

Figure 30. Rise in Soil Temperature for Wet Soil at a 2-m Depth.
The figure shows the predicted rise in soil temperature versus time at a depth of 2 m using wet-soil thermal properties. (DTN: LABR150191DN99.001)

5. CONCLUSIONS

We divide the conclusions of the present study into two groups: those from the site-scale thermohydrologic simulations and those from soil-zone thermal modeling. The site-scale thermohydrologic simulations revealed the following major conclusions (additional analyses not directly pertinent to the soil-zone temperature were discussed but are not listed here):

- The waste heat from the potential repository has its greatest impact on the heat flux reaching the soil zone directly above and in the center of the potential repository and tapers off to ambient heat-flux conditions within 500 m of the edge of the repository.

- Topographic influence has a noticeable but relatively minor effect on the spatially varying surface heat flux. The nature of this effect is shown in Figure 12 with the maximum heat flux occurring somewhat to the east of the center of the repository due to the shorter distance from the heat source to the surface at this location.

- Infiltration rate, the nature of heat transfer at the water table, and the details of near-field thermohydrologic processes all have very small influence on the predicted heat flux to the soil zone. The results are dominated by the heat load versus time (dependent on the details of the heat-loading strategy) and the large-scale unsaturated-zone heat-transfer processes of thermal conduction and convection. Regarding infiltration rate, the direct influence at a given set of thermal properties is small because the heat-carrying capacity of the downward-percolating fluid is small compared to the repository heat source. Of course, infiltration rate will indirectly impact soil-zone temperature profiles through the influence of water content on the thermal properties of the soil (see below).

- Time-varying heat flux at the surface will exhibit behavior similar to that in Figure 13 with discernible increases in heat flux occurring after about 200 yr, reaching a maximum after about 1000 yr, and slowly declining to ambient, pre-emplacement conditions within 100,000 yr.

- Predicted heat flux at the surface is considerably enhanced when simulations are carried out with thermohydrologic effects, compared to heat-conduction-only solutions. The heat-pipe effect in the thermohydrologic simulations transports heat preferentially upward, resulting in larger heat losses from the mountain to the atmosphere.

- The maximum surface heat flux predicted for the repository design conditions chosen for examination (83 MTU/acre, 70,000 MTU total) was about 900 mW/m^2, compared to ambient values of order 35 mW/m^2. Three-dimensional simulations yield somewhat lower maximum values due to spreading of heat in all directions. We used the results of the two-dimensional, thermohydrologic model for conservatism (i.e., to obtain the maximum possible soil-temperature rise). The predicted value was shown scaled linearly with areal mass loading (i.e., MTU/acre).

From the analyses of the one-dimensional soil-zone simulations, we make the following conclusions and recommendations:

- Current predictions are somewhat uncertain due to uncertainties in the thermal properties of the soil, particularly thermal conductivity and, hence, thermal diffusivity.

- Analyses based on conventional soil heat-conduction models indicate that the original time scale of the measurements collected at the site (weekly to monthly) could not be used to accurately estimate the soil thermal conductivity for the sampling depths chosen (15, 30, and 45 cm). Damping depths for seasonal variations (observed in the temperature measurements to date) are much greater than the sampling depths, making it impossible to observe amplitude or phase shifts predicted for thermal response, which can, in principle, provide sensitive estimates of soil thermal diffusivity.

- Therefore, we recommended that the time period of sampling be reduced to allow us to analyze the response to diurnal temperature fluctuations. Alternatively, the depth of the sampling ports could have been increased. However, this approach was impractical because the soil thickness is less than one meter in many locations. Furthermore, measurements over constrained time intervals (say, one week) would allow the influence of infiltration events (and presumably wetter soil conditions during the measurements) on thermal properties to be measured readily. With dependable, field-scale measurements of soil-zone thermal properties at various soil moisture contents, much tighter constraints on the predicted soil temperatures in response to repository heat would then be possible.

- Analysis of the frequency response of the measured thermal signals over a 10-day period allowed us to use the diurnal fluctuations to estimate the thermal diffusivity of the soil during the measurement period. Specifically, the phase shift of the diurnal temperature cycle was clearly lagged at the subsurface measuring position, which allowed us to easily estimate the thermal diffusivity, assuming a thermal-conduction model. The value so obtained was very close to the estimated soil thermal diffusivity under wet conditions.

- Despite some residual uncertainty, it is still possible to predict the average temperature rise in the soil and its time variability. This was done by estimating thermal properties for soils of different moisture contents. For example, Figure 30 is the prediction for average temperature rise at 2-m depth for thermal properties predicted for a "measured soil." The maximum in this case is 0.8°C, and the long-term time variation mirrors the predicted heat-flux curves generated for the repository in the site-scale simulations. Recall that this thermal conductivity was found to be approximately equal to the value predicted for a "wet" soil. In theory, a partially saturated soil has a predicted thermal conductivity that varies with moisture content, so it is possible that, during drier periods, the temperature rise would be greater than 0.8°C. Field-scale calibration under different soil-moisture conditions would likely reveal some soils with lower thermal conductivities and higher predicted temperature rises. However, the available data suggest very modest temperature rise due to repository heat effects. Note also that the predicted temperature rise is linear with depth. Whether this level of thermal perturbation from the ambient

system is sufficient to significantly change the ecosystem is beyond the scope of the present study. We present the results to provide reliable bounds to those responsible for assessing the environmental impact of the waste heat.

- When this repository heat flux is applied to a system exhibiting seasonal variations in soil temperature, the effects can be superimposed. Similar damping depths and soil-temperature response curves are predicted, with the mean value that is now dependent on depth.

- The heat exchange between the atmosphere and the soil surface is probably efficient enough that the temperature at the surface can be assumed to be equal to the atmospheric temperature. This result is based on a natural air-convection heat-transfer analysis, which is likely to significantly underestimate the heat-transfer coefficient, thereby maximizing the temperature difference between the air and soil surface. The result simplifies the analysis by eliminating one additional heat-exchange process from consideration. However, the result must be viewed in light of the analysis of the difficulties in interpretation of some of the field data. Temporary snow cover, or regions with significant radiative heating effects, must ultimately be considered when assessing the thermal effects of heat at a particular time and location.

6. REFERENCES

Bennett, C.O., and Myers, J.E. 1974. *Momentum, Heat, and Mass Transfer*. New York, NY: McGraw-Hill Book Company.

Bish, D. L. 1995. Thermal behavior of natural zeolites. In *Natural Zeolites '93*, edited by Ming, D.W., and Mumpton, F.A., pp. 259–269. Brockport, NY: International Communications. TIC 217195.

Buscheck, T.A., and Nitao, J.J. 1993. Repository-heat-driven hydrothermal flow at Yucca Mountain: Part I. Modeling and analysis. *Nuclear Technology*, 104 (3), 418–448. Hinsdale, IL: American Nuclear Society. TIC 224039.

Buscheck, T.A., Nitao, J.J., and Ramspott, L.D. 1996. Localized dryout: An approach for managing the thermal-hydrological effects of decay heat at Yucca Mountain. *Materials Research Society Symposium Proceedings*, 412, 715–722. Pittsburgh, PA: Materials Research Society. TIC 235933.

Carslaw, H.S., and Jaeger, J.C. 1985. *Conduction of Heat in Solids*, second edition. New York, NY: Oxford University Press. TIC 4796.

CRWMS M&O (Civilian Radioactive Waste Management System Management and Operating Contractor). 1995. *Total System Performance Assessment—1995: An Evaluation of the Potential Yucca Mountain Repository*. B00000000-01717-2200-00136, Rev. 01. Las Vegas, Nevada: Author. TIC 224028.

Flint, A.L., Hevesi, J.A., and Flint, L.E. 1996. *Conceptual and Numerical Model of Infiltration for the Yucca Mountain Area, Nevada: U.S. Geological Survey Yucca Mountain Project Milestone Report 3GUI623M*. U.S. Geological Survey Water Resources Investigation Report. Denver, CO: U.S. Geological Survey. MOL19970409.0087.

Hillel, D. 1980a. *Fundamentals of Soil Physics*. New York, NY: Academic Press. TIC 215655. HQS.19880517.1776.

Hillel, D. 1980b. *Applications of Soil Physics*. New York, NY: Academic Press. TIC 217649.

Hillel, D. 1982. *Introduction to Soil Physics*. New York, NY: Academic Press. TIC 215629.

Loeven, C. 1993. A summary and discussion of hydrologic data from the Calico Hills nonwelded hydrogeologic unit at Yucca Mountain, Nevada. Los Alamos National Laboratory report LA-12376-MS. Los Alamos, NM: Los Alamos National Laboratory. TIC 205254. NNA.19921116.0001.

Marshall, T.J., and Holmes, J.W. 1979. *Soil Physics*. Melbourne, Australia: Cambridge University Press. TIC 240992.

Nitsche, H., Roberts, K., Prussin, T., Muller, A., Becraft, K., Keeney, D., Carpenter, S.A., Gatti, R.C. 1994. Measured solubilities and speciations from oversaturation experiments of neptunium, plutonium, and americium in UE-25 p#1 well water from the Yucca Mountain Region: YMP milestone report 3329. Los Alamos National Laboratory report LA-12563-MS. Los Alamos, NM: Los Alamos National Laboratory. NNA.19931015.0073

Pruess, K., Wang. J.S.Y., and Tsang, Y.W. 1990. On thermohydrologic conditions near high-level waste emplaced in partially saturated fractured tuff: 1. Simulation studies with explicit consideration of fractures effects. *Water Resources Research*, 26 (6), 1235–1248. Washington, DC: American Geophysical Union. TIC 221923.

Robinson, B.A., Wolfsberg, A.V., Zyvoloski, G.A., and Gable, C.W. 1995. An unsaturated-zone flow and transport model of Yucca Mountain. Los Alamos National Laboraroty YMP milestone 3468. Los Alamos, NM; Los Alamos National Laboratory. TIC 236605. MOL.19980213.0091.

Robinson, B.A., Wolfsberg, A.V., Viswanathan, H.S., Gable, C.W., Zyvoloski, G.A., and Turin, H.J. 1996. Modeling of flow, radionuclide migration, and environmental isotope distributions at Yucca Mountain. Los Alamos National Laboratory YMP milestone 3672. Los Alamos, NM; Los Alamos National Laboratory. TIC 233142. MOL.19970103.0042.

Robinson, B.A., Wolfsberg, A.V., Viswanathan, H.S., Bussod, G.Y., Gable, C.W., and Meijer, A. 1997. The site-scale unsaturated-zone transport model of Yucca Mountain. Los Alamos National Laboratory YMP milestone SP25BM3. Los Alamos, NM; Los Alamos National Laboratory. MOL.19980203.0570.

Ross, B., Amter, S., and Lu, N. 1992. Numerical studies of rock-gas flow in Yucca Mountain. Sandia National Laboratories report SAND 91-7034. Albuquerque, NM: Sandia National Laboratories. TIC 204094.

Sass, J.H., Lachenbruch, A.H., Dudley, W.W., Priest, S.S., and Munroe, R.J. 1988. Temperature, thermal conductivity, and heat flow near Yucca Mountain, Nevada: Some tectonic and hydrologic implications. U. S. Geological Survey Open-File Report 87-649. Flagstaff, AZ: U.S. Geological Survey. TIC 203195.

Thomson, W. (Lord Kelvin). 1861. On the reduction of observations of underground temperature; with application to Professor Forbes' Edinburgh observations, and the continued Calton Hill series. *Transactions of the Royal Society of Edinburgh*, 22, 405–427. Edinburgh, Scotland: The Society.

Viswanathan, H.S., Robinson, B.A., Valocchi, A.J., and Triay, I.R. 1998. A reactive transport model of neptunium migration from the potential repository at Yucca Mountain. *Journal of Hydrology*, 209, 251–280. Amsterdam, Netherlands: Elsevier Science B.V.

Wittwer, C., Chen, G., Bodvarsson, G.S., Chornak, M., Flint, A., Flint, L., Kwicklis, E., and Spengler, R. 1995. Preliminary development of the LBL/USGS three-dimensional site-scale model of Yucca Mountain, Nevada. Lawrence Berkeley Laboratory report LBL-37356/UC-814. Berkeley, CA: Lawrence Berkeley National Laboratory. TIC 221218.

APPENDIX

DETERMINATION OF DIFFUSIVITY

INTENTIONALLY LEFT BLANK

Table 1. Diffusivity Derived from Soil and Air Temperatures

Site	Probe	Lag Time (hr)	Inferred Diffusivity ($\times 10^{-7} m^2 s^{-1}$) Based on:	
			Lag of Response	Amplitude of Response
1	1	13	6.36	13.0
1	2	13	6.36	9.7
1	3	13	6.36	10.1
2	1	14	5.48	9.4
2	2	16	4.20	8.5
2	3	16	4.20	8.1
5	3	12	7.46	11.6
6	1	12	7.46	12.0
7	1	14	5.48	9.0
8	4	15	4.77	8.4
	Avg.	13.8	5.81	9.98
	Std. Dev.	1.48	1.19	1.68

Avg.: average Std. Dev.: standard deviation

(DTN for temperature data used in these analyses is MO9812PSNTGH45.000.)

As discussed in the main text of this document, the diffusivity in the last two columns of Tables 1 through 4 of this appendix were calculated as follows. The diffusivity in the "Lag of Response" column was calculated from the τ_l values in the "Lag Time" column using Eq. 10 in the main text (and assuming that $z = 0.45$ m and $\tau_{24} = 24$ hr). The diffusivity in the "Amplitude of Response" column was calculated from the measured amplitude of the variations in the temperature-time series using Eq. 14 in the main text.

Table 2. Diffusivity Derived from Winter Soil and Air Temperatures, December 1997

Site	Probe	Lag Time (hr)	Inferred Diffusivity ($\times 10^{-7} m^2 s^{-1}$) Based on:	
			Lag of Response	Amplitude of Response
5	1	8	16.8	10.9
5	2	11	8.88	8.2
5	3	–	–	–
3	1	–	–	–
3	2	12	7.46	12.0
3	3	13	6.36	8.8
2	4	–	–	–
2	5	13	6.36	13.1
2	6	12	7.46	14.3
1	1	–	–	–
1	2	11	8.88	13.0
1	3	11	8.88	14.4
	Avg.	11.38	8.89	11.84
	Std. Dev.	1.60	3.37	2.36

Avg.: average Std. Dev.: standard deviation

(DTN for temperature data used in these analyses is MO9812PSNTGH45.000.)

Table 3. Diffusivity Derived from Winter Soil and Air Temperatures, January 1998

Site	Probe	Lag Time (hr)	Inferred Diffusivity ($\times 10^{-7} m^2 s^{-1}$) Based on:	
			Lag of Response	Amplitude of Response
5	1	4	67.2	181.4
5	2	2	268.6	24.7
5	3	2	268.6	24.7
3	1	–	–	–
3	2	2	268.6	7.5
3	3	2	268.6	4.6
2	4	10	10.8	2.8
2	5	11	8.88	2.3
2	6	11	8.88	2.7
1	1	8	16.8	4.6
1	2	9	13.3	3.4
1	3	9	13.3	3.3
	Avg.	6.36	109.4	23.8
	Std. Dev.	3.93	127.3	52.9

Avg.: average Std. Dev.: standard deviation

(DTN for temperature data used in these analyses is MO9812PSNTGH45.000.)

Table 4. Diffusivity Derived from Winter Soil and Air Temperatures, February 1998

Site	Probe	Lag Time (hr)	Inferred Diffusivity ($\times 10^{-7} m^2 s^{-1}$) Based on:	
			Lag of Response	Amplitude of Response
5	1	6	29.8	20.4
5	2	8	16.8	7.4
5	3	8	16.8	7.4
3	1	–	–	–
3	2	9	13.3	10.1
3	3	10	10.8	5.9
2	4	9	13.3	10.3
2	5	11	8.88	8.8
2	6	10	10.9	9.2
1	1	8	16.8	15.9
1	2	9	13.3	10.5
1	3	9	16.8	11.9
	Avg.	8.7	15.2	10.7
	Std. Dev.	1.3	5.6	4.2

Avg.: average Std. Dev.: standard deviation

(DTN for temperature data used in these analyses is MO9812PSNTGH45.000.)